Inclusions in clinopyroxene megacrysts from Marion Island

by

Keabetswe Dimakatso Lehong

Submitted in partial fulfilment of the requirements for the degree

MASTER OF SCIENCE IN GEOLOGY

In the Faculty of Natural & Agricultural Sciences

University of Pretoria

Pretoria

2016-12-02

ABSTRACT

Marion Island is a sub-Antarctic island which lies 300 km south of the South West Indian Ridge. The island is extensively affected by two periods of volcanism with the oldest erupting during the Pleistocene and the younger during the Holocene period. This study focused on inclusions present within several enormous megacrysts retrieved from a scoria cone on Marion, named Pyroxene Hill. Microfocus CT, electron microprobe, and Raman spectroscopy are used to identify all the mineral phases present within the clinopyroxene megacrysts as well as to determine their textural relationships in order to visualise their internal features without obliterating any of these rare megacrysts. Inclusions of olivine, Fe-Ti-Al-Cr oxides (magnetite, chromite, and ilmenite), rhomb oxides (hematite) and sulphides were identified. Amphibole was also identified as secondary product. Their textural relationships are used to determine the major magmatic processes and formation mechanisms influencing their formation and preservation. Dehydrogenation-oxidation process was found to be the primary magmatic process driving the formation of mineral phases present. Water was also identified as a crucial phase required in the magmatic system to accelerate rapid growth of the clinopyroxene megacryst.

ACKNOWLEDGEMENTS

I would first like to express my sincere gratitude to my supervisor Dr. James Roberts for the continuous support, guidance and patience during my M.Sc. studies. His immense knowledge and unfading guidance motivated me in writing my dissertation. My sincere thanks also goes to my Co-Supervisor Dr. Gelu Costin who instilled in me a love for minerals and exposure to various research facilities. Without your valuable support, it would not be possible to conduct this research. I would also like to show gratitude to Dr. Frikkie De Beer, Lunga Bam, and Jakobus Hoffman who gave access and assistance to Micro-focus X-ray tomography facility (UID: 72310) and for sharing their expertise, guidance and encouragement when using the facilities. I take this opportunity to express gratitude to all the members of the Geology Department for their help and support. Last but not the least; I would like to thank my family: my husband, precious daughter, my parents and my sisters for supporting me spiritually throughout writing this thesis. I could have not imagined a better support system than this.

DECLARATION OF ORIGINALITY

UNIVERSITY OF PRETORIA

Full names of student: Keabetswe Dimakatso Lehong

Student number: u29484317

Subject of the work: Inclusions in clinopyroxene megacrysts from Marion Island

Declaration

I, Keabetswe Dimakatso Lehong declare that the dissertation, which I hereby submit for the degree Master of Science in Geology at the University of Pretoria, is my own work and has not previously been submitted by me for a degree at this or any other tertiary institution.

SIGNATURE: _____

DATE: 02-12-2016

TABLE OF CONTENTS

LIST OF TABLES

LIST OF FIGURES

CHAPTER 1 – GENERAL INTRODUCTION

The cycling of material within the Earth's interior has a profound effect on the growth and evolution of oceanic islands dotted across the world. Through the constant and continuous transfer of heat from the outer core and inner mantle, the mantle-derived material is steered through the Earth's interior and, in other instances, discharged to the Earth's surface along injector paths and fractures as buoyant melt migrates upward. These extrusive products are often preserved along the islands' landscapes and provide important evidence critical in understanding how the Earth's heat engine functions. They also allow us to establish the processes which lead to the eruption. Megacrysts of clinopyroxene have also become recurrent extrusive products of many volcanic deposits across the world. These large crystals are often associated with alkaline basaltic lavas and may often be accompanied by peridotite and pyroxenite xenoliths (Woodland & Jugo, 2007). Marion Island hosts clinopyroxene megacrysts in several scoria cones dotted around the island. These hold a record of the island's magmatic history as well as evidence of the processes at play during their formation. Studying its eruptive behaviour, melt migration and chemical composition of samples collected from the scoria cone may potentially assist in determining the rate at which the megacrysts evolved as well as their residence history in the magma chamber.

1.1. Positioning of Marion Island

Marion Island together with Prince Edward Island makes up the Prince Edward Island Group of the Southern Indian Ocean. These are relatively young islands with a lifespan of less than 1 My (McDougall *et al.*, 2001). Marsh (1948) gave a poetic account of his first sighting of the island describing its landscape and geology as follows:

"She rose, a jade jewel, out of the sea. Her lush green coat was fringed with the black lace of the cliffs and her heights draped in scintillating snow."

The Prince Edward Islands together with South Georgia, South Sandwich, Iles Crozet, Kerguelen, Bouvet, Heard and McDonald islands are the only land masses located within the 40^{o} and 60^{o} South latitudes of the Southern Ocean (Bergstrom *et al.*, 2006). The islands are in close proximity to each other and are arranged in a sub- Antarctic volcanic chain (Figure 1.1).

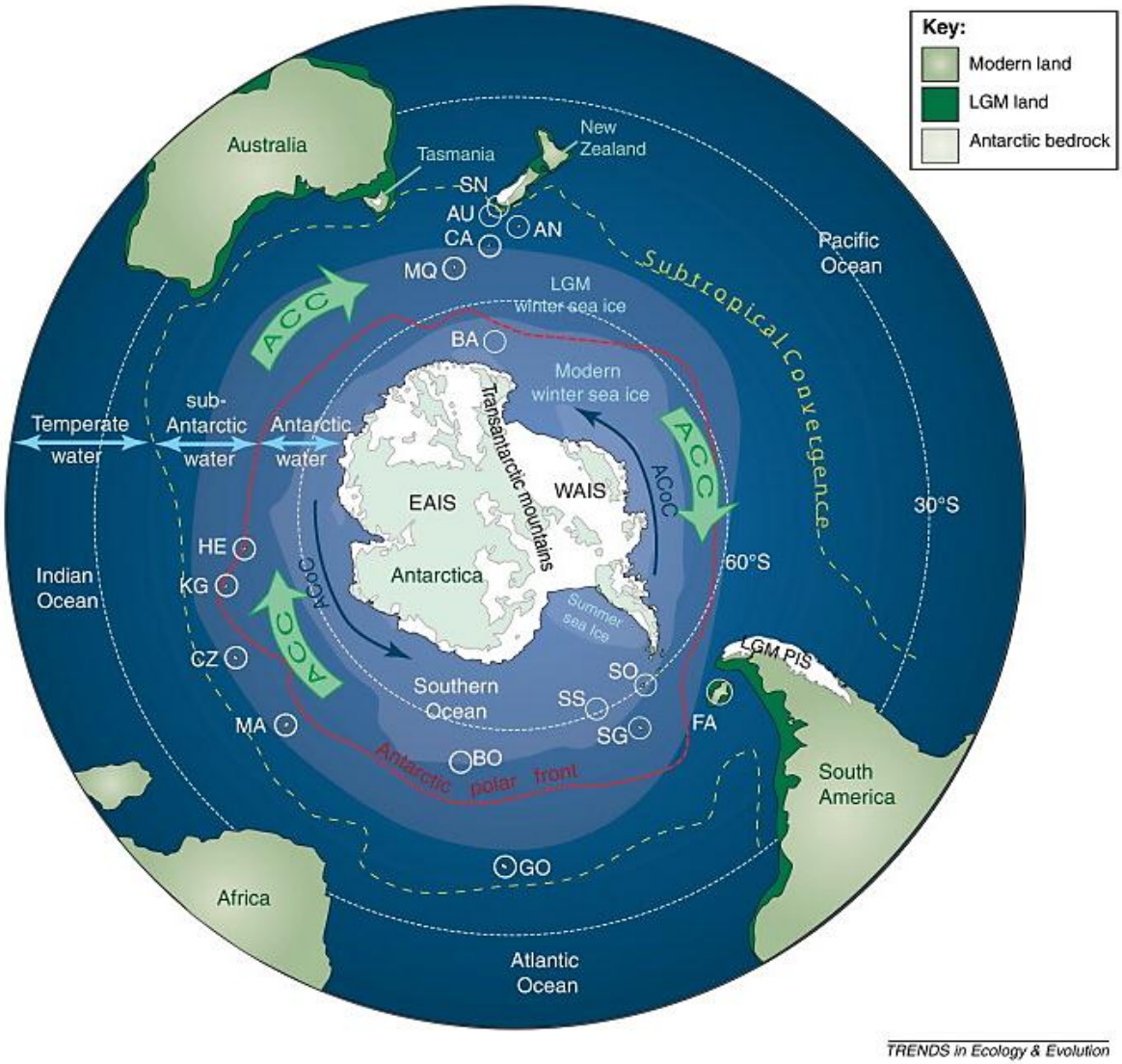

Figure 1. 1: The positioning of the Antarctic Peninsula (centre) with its surrounding islands. Also shown are islands located in the South Indian Ocean between the 40° and 60° South latitudes (Prince Edward, Crozet, Heard, St Paul, and Kerguelen island) (Fraser *et al.*, 2012).

Marion Island, located at 46°54'S, 37°45'E, is a sub-Antarctic island which lies 300km south of the Southwest Indian Ridge (McDougall *et al.*, 2001; Hall *et al.*, 2011). It lies adjacent to Prince Edward Island, and both islands emerge from a flat-topped submarine highland as shield-like volcanic edifices (Boelhouwers *et al.*, 2008). The island's aerial extent is about 293km^2 and it stretches to about 19km in length (SANAP, 2015a). Its highest peak climbs to 1230m and is covered by enduring ice sheets and snow (Figure 1.2). The island is classified as a Hawaiian-type volcano as relicts of a shield volcano are speckled across its topography (Mahoney *et al.*, 1992). Marion Island is considered a hotspot volcano as it is

situated at the tip of an ocean intraplate boundary within the Antarctic and African tectonic plates. Numerous studies suggest that it is part of a hot-spot track which extends to the east coast of Madagascar, a volcanic chain formed as a moving plate shifts across a relatively stationary plume. Madagascar formed the focal point of the plume and is also responsible for separating Great India from Madagascar 88 My ago (Storey *et al.*, 1995).

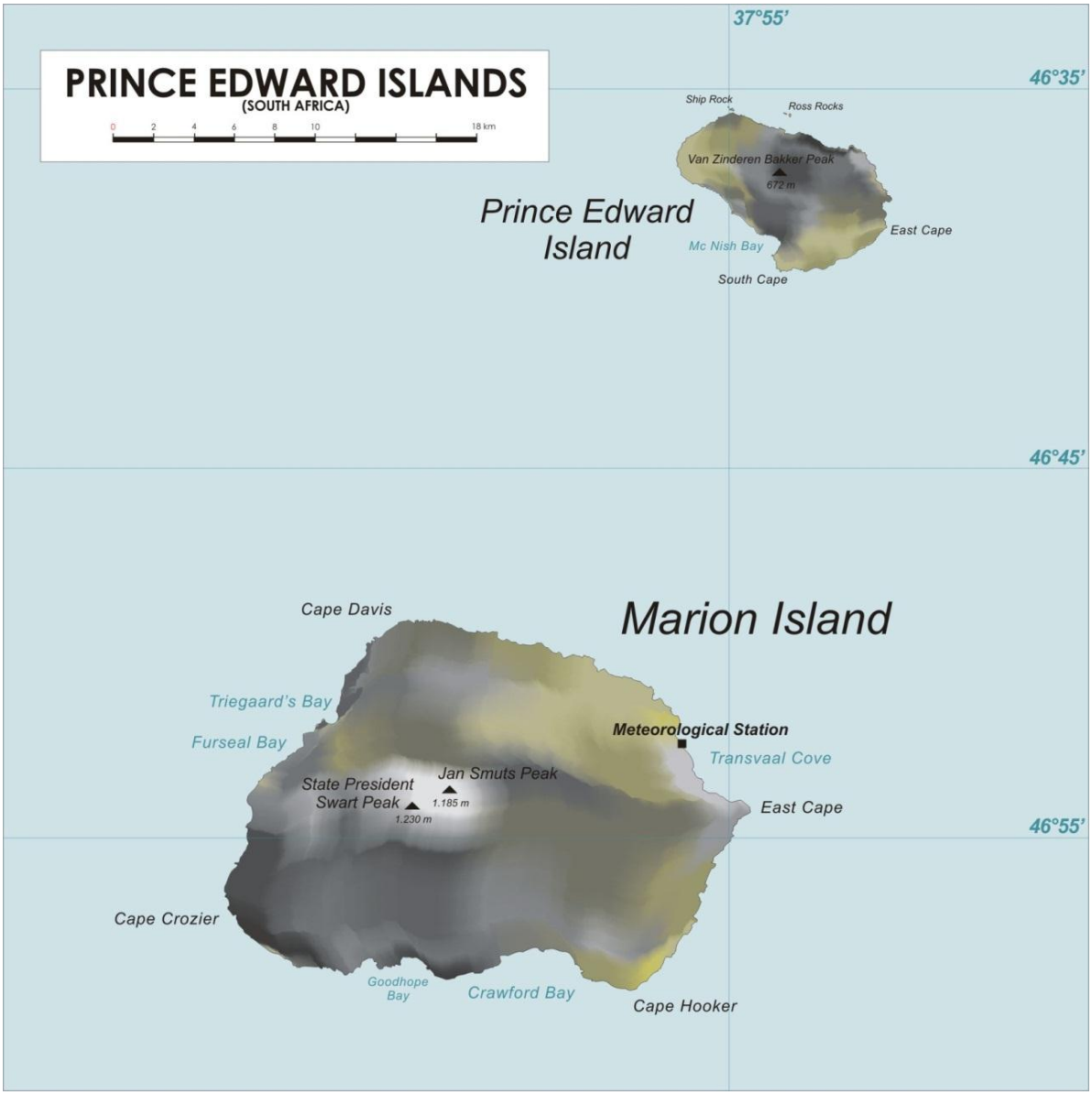

Figure 1. 2: Positioning of Marion Island relative to South Africa and Prince Edward Island (SANAP, 2015a).

1.2. Historical background of Marion Island

At the time of its accidental discovery by the Dutch ship, Maerseveen, in the late 1600s (SANAP, 2015b), no attempt was made to land on the island. It was then rediscovered by a French explorer named Marion du Fresne whilst in pursuit of discovering the Southern continent (SANAP, 2015b). It took another five years for another explorer to come across and officially annexe the islands. Captain James Cook named both the islands Prince Edward Islands but later changed the name of the bigger island to Marion to pay tribute to Marion du Fresne (Potgieter and duPlessis, 1970). The South African flag was later hoisted on the island by Governor General G. Brand van Zyl on 4 January 1948 when annexed to fall under Cape Town and the the administration of the Western Cape Province (Hutson, 2003).

Economically, early shippers and sealers were attracted to the rich biodiversity of birdlife and seals on the island. This resulted in the unrestrained exploitation of elephant seals for oil and fur (Green, 1965), ultimately resulting in them almost becoming extinct locally (Hofmeyr *et al.*, 1997; Cooper and Headland, 1991). This eventually sparked concerns over the biological welfare of animals on the island which resulted in the halting of most harvesting activities by the early 1900s.

Considerable efforts aimed at protecting the diverse birdlife, penguins and albatross species found on the island eventually led to the declaration of Marion Island as a Special Nature Reserve in 1995 under the Environment Conservation Act, Act No. 73 of 1989 (Hutson, 2003). A management committee has been set in place by the Department of Environmental Affairs of South Africa to monitor and protect the fragile ecosystem of the island and to also engage and attract scientists to conduct numerous researches on the islands. Research on Marion Island is primarily focussed on weather and climate studies, the collaboration between marine and terrestrial systems, the life histories of seals, seabirds and killer whales, the life histories of birds found on Marion, the formative framework and functionality of terrestrial and near-shore ecosystems (SANAP, 2015c). The numerous research programmes have since been moved to the Department of Science and Technology under the supervision of the National Research Foundation with new scientific structures and policies set in place. A meteorological station has also been erected on Marion Island which serves as a world-class weather forecasting unit for South Africa. It has played a major role in

the differentiation of the mid- latitudinal climate as well as the provision of a substantial amount of evidence for change in climatic conditions over the Southern Indian Ocean (le Roex and McGeoch, 2008; Boelhouwers *et al.*, 2008).

1.3. Land surface processes/ geological background

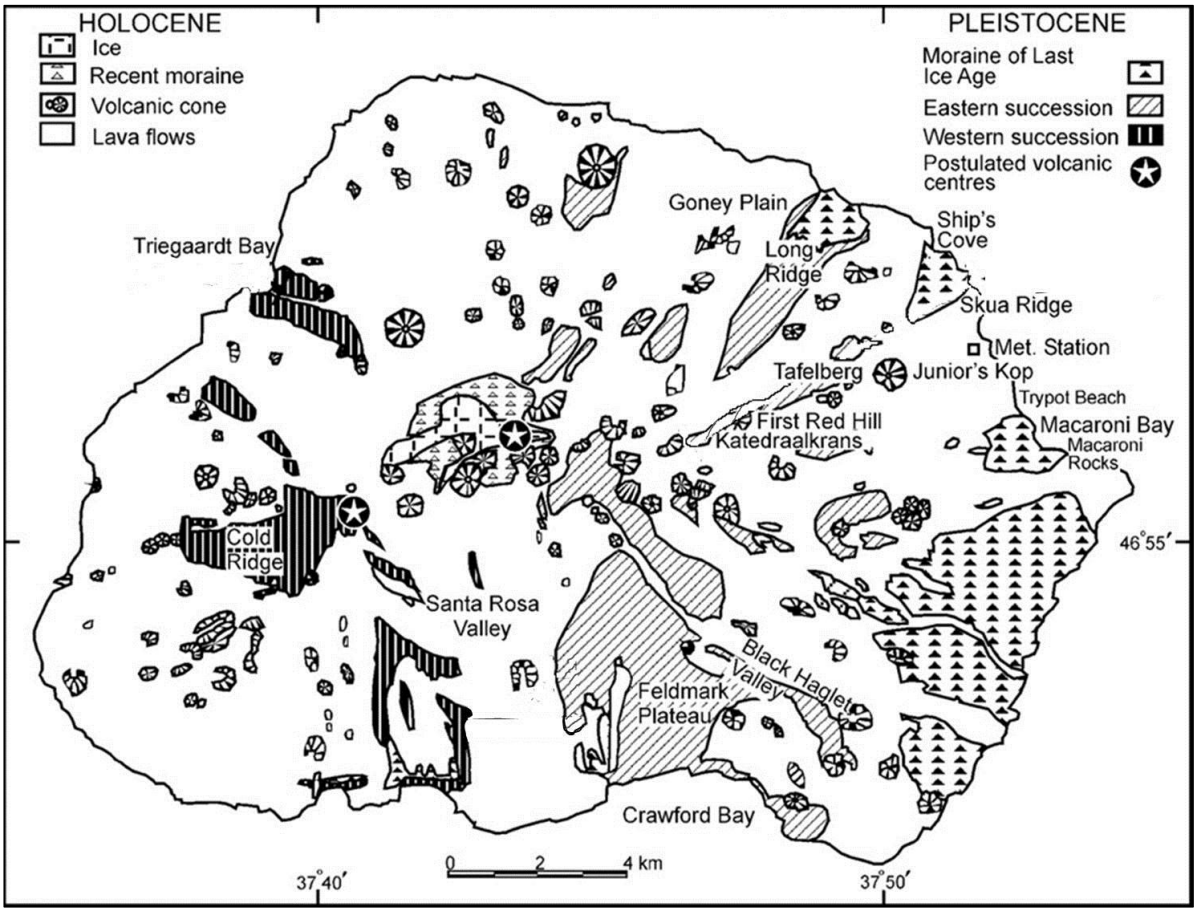

Figure 1. 3: A simplified geological map of Marion Island, showing its volcanic and glacial evidence that assists in differentiating the two eruptive periods of the island (Holocene and Pleistocene). Taken from McDougall *et al*. (2001).

Marion island is extensively affected by two periods of volcanism: the oldest eruptions during the Pleistocene (2.6-0.01 Ma), which are masked by the younger lavas which erupted during the Holocene (< 0.01 Ma) (Figure 2.2). Geological investigations have revealed that the earliest eruptive period is associated with a succession of grey lavas, which in turn correlate with alkaline basalts, pyroclastic beds and intercalated till (Verwoerd *et al.*, 1981).These older Pleistocene lavas are also typified as having distinct westerly and easterly flows and also show indentations of glaciations, hence making the Pleistocene eruptions a contemporary event that took place during the interglacial period. The younger black lavas

are predominantly composed of blocky lava, a'a and pahoehoe flows, and subsequently, lead to the formation of copious scoria cones and tuff cones which conceal evidence of the preceding glacial event (Verwoerd, 1971; McDougall *et al.*, 2001). The mineralogical composition of the black lavas is fairly identical to that observed in the grey lavas (Verwoerd *et al.*, 1981). The grey lavas are characterised by minerals such as olivine, alkali feldspar, pyroxene ±plagioclase, whereas the black lavas (and the Red Scoriae) have spinel as an additional phase (Prinsloo *et al.*, 2010).

Volcanic ash deposits with compositions similar to that of basaltic rocks have also been identified on the island. Marion Island can thus be classified as a typical example of ocean island basalts (McDougall *et al.*, 2001). Plotting representative samples of these rocks on a total alkali vs. silica (TAS) diagram indicates that they form a typical alkaline series (Figure 1.4).

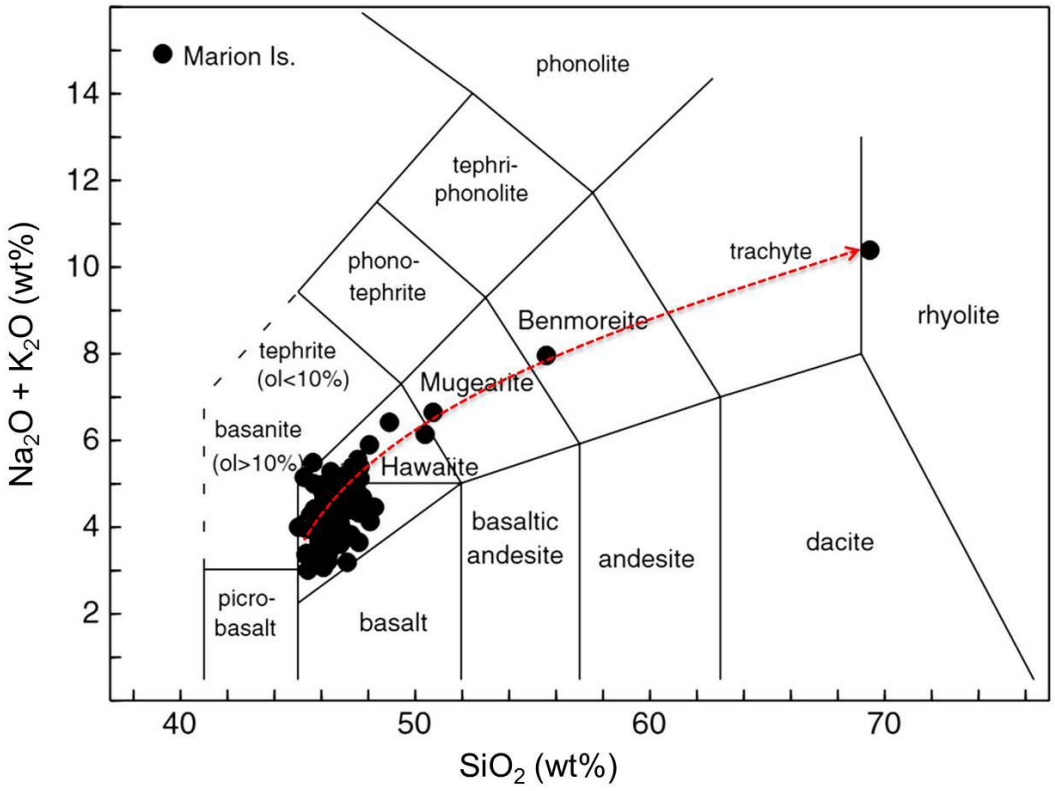

Figure 1. 4: A total alkali-silica (TAS) diagram for a sample suite consisting of volcanic rocks from Marion Island. The samples typically form an alkaline series, as indicated by the red arrow (le Roex *et al.*, 2012).

Marion Island is considered an active volcanic centre. Its surface topography is sectioned by radial faults with erupting centres emerging as scoria cones along the fault planes (Verwoerd, 1971; Hall, 2002). Previous studies hypothesise that volcanism on the island is triggered by changes in isostatic rebound due to the unloading of ice at the end of the Last Glacial Maximum (Hall, 1982; 2002). This unloading is further believed to have initiated the formation of thrust faults in areas covered with thick layers of ice (Hall, 1982).

A comprehensive study on the nature of these eruptive centres is supplemented by the re-evaluation of the proposed fault structures, volcanic rocks and the disseminated palaeo-glacial material exposed along the escarpments. Detailed field investigations of the much anticipated fault structures revealed that erosional scarps were mistaken for thrust faults (Hall *et al.*, 2011). This finding is supported by the lack of major fault indicators such as breccia or cataclasite (Hall *et al.*, 2011). Although evidence of slickensides, identified in the black and grey lavas, does prove that there is active faulting on the island, a mere 2mm variance in direction of movement and fault displacement of as little as 2 mm cannot account for the dislodgement that will cause the formation of escarpments on Marion Island (Hall *et al.*, 2011). It is further argued that the perception that volcanism is stimulated by deglaciation is rather improbable when adapting Anderson's theory of faulting (Anderson, 1951; Hall *et al.*, 2011). In order for normal faults to form, the principal stress (σ_1) should be vertical with fractures dipping at an angle more than 45° (Suppe, 1985). This arrangement triggers a down-dipping slip, thus creating grounds for horizontal extension. However, as in the case on Marion Island, isostatic alteration leads to the vertical extension during the unloading of glacial ice (Hall *et al.*, 2011). Thus, it can be resolved that the orientation of principal stresses and the lack of horst and graben structures on Marion Island are an unbefitting configuration for the formation of normal faults (Hall *et al.*, 2011).

Volcanism on Marion Island has always been episodic. This observation is supported by the occurrence of unconformities and time gaps in the geologic sequence and rocks dated within the past 500 thousand years. McDougall *et al.* (2001) reconstructed the geochronology of Marion Island and identified in total, eight periods of volcanism using K-Ar age dating (Figure 1.5). These are as follows:

Period I – Ages from 450 ±4 ka at the base of the sequence to 418 ±5 ka at the uppermost part of the sequence. It is only present in the Santa Rosa Valley and consists of eight successive subaerial lava flows.

Period II – An average age of 350 ka was determined from a flow that overlies and is 3 km south of the sequence identified at the Santa Rosa Valley. This sequence also rests directly on top of an unconformity at Crawford Bay.

Period III - A basal flow located at Ship's Cove together with a coastal outcrop at Macaroni Bay gave an age of 240 ka.

Period IV – Nine age determinations were run for three broadly-spaced localities (Macaroni, Ship's Cove, and Triegaardt Bay) giving an age of about 170 ka.

Period V – A succession of lava flows located between Skua Ridge and Tafelberg gave an approximate age of about 110 ka.

Period VI – Two lava flows from Santa Rosa Valley and Triegaardt Bay were sampled and analysed giving an approximate age of 85 ka. These flows unconformably overlie the above-mentioned sequence and cut through the older rocks at an angle. Though the distance between the two localities is large, this might mean that this volcanic episode is wide-spread.

Period VII – Lavas positioned at higher altitude on the island make up this sample suite. More than 15 age determinations were conducted and have given an average age of 50 ka.

Period VIII – This sample suite is made up of the Holocene black lavas and represents volcanism to date on the island. These lavas erupted after the Last Glaciation and overlie glacial moraines. An approximate K-Ar age of <10 ka was determined.

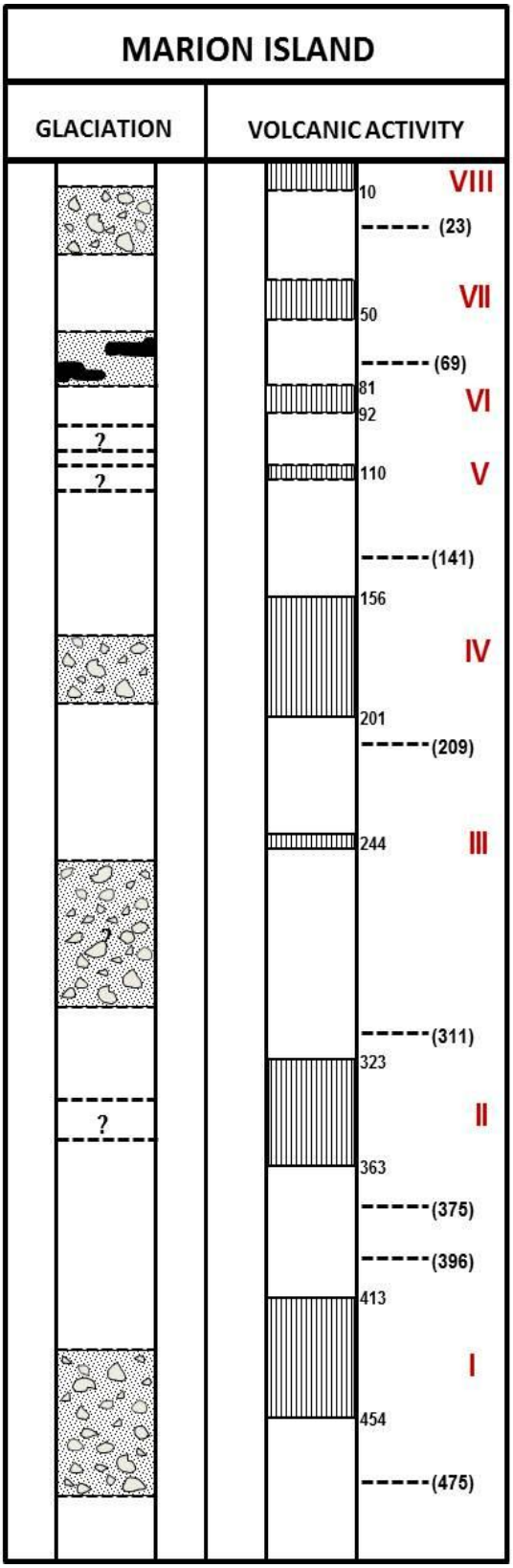

Figure 1. 5: The chronology of glacial and volcanic rocks of Marion Island (McDougall *et al.*, 2001).

Marion is the only island among the Prince Edward Islands which still has its glacial record preserved (Boelhouwers *et al.*, 2008). A glaciation period dated at 50000-15000 years

separates the two eruptive periods of the island (le Roex *et al.*, 2012). The evidence is much more noticeable in the older Pleistocene grey lavas, despite having most of the deposits buried beneath a succession of lava flows (Verwoerd *et al.*, 1981; Boelhouwers *et al.*, 2008). This burial limits the visibility of older flows to areas with coastal cliffs, escarpments and rivulets, showing evidence in the form of striations, glacial till, intra-glacial lavas and fluvioglacial deposits (Hall, 1982; McDougall *et al.*, 2001). Previous studies related to Marion's glacial history revealed only three glacial periods, but technological advancements in K-Ar age determination of volcanic materials from Marion Island has permitted scientists to further investigate the geochronology of intercalated glacial tills (Boelhouwers *et al.*, 2008). In addition to the three cold periods identified by Hall (1982), the total number of glacial periods has now been revised to five (McDougall *et al.*, 2001), as shown in Figure 1.5.

1.4. Problem statement

There is very little detailed geological literature available on Marion Island. This is amplified by extreme sampling restrictions on the island, thus resulting in a significant gap of knowledge and research aimed at understanding the geological evolution of the island. This study focuses on a small set of giant clinopyroxene megacrysts provided by previous visitors to the island.

1.5. Aims and objectives

The objective of this research is to determine the various types of inclusions present within the sampled clinopyroxene samples and to provide new data for these crystals using various analytical tools. The study is also aimed at understanding the physical, chemical and morphological properties of the inclusions present. This is also geared towards determining any morphological or chemical changes to the clinopyroxene megacrysts during magma ascent. This will assist in the creation and evaluation of its evolution history and in determining the magmatic processes responsible for the formation and preservation of the inclusions present. Ultimately, we will determine what processes led to the formation of the megacrysts.

1.6. Research approach

In order to meet the set aims and objectives, numerous assessments needed to be carried out. The first set of assessments is used to determine the mineralogy and morphological properties of inclusions present within the megacrysts using a microfocus X-ray computed tomography (µCT). Pore size distribution and the surface area of the samples will also be determined. The second set of assessment involves the characterisation of minerals present using Scanning Electron Microscopy (SEM), Electron Probe Microanalysis (EPMA) and Raman spectroscopy. This is crucial in laying out the mineralogical constraints on the origin of the mineral phases present and in identifying the processes and conditions of formation necessary to crystallise such large crystals. This will also involve making comparisons between clinopyroxenes and olivines derived from both a mantle source and crustal source. Lastly, the effect of water, oxygen fugacity and pressure and temperature constraints leading to their formation will be addressed.

CHAPTER 2 – LITERATURE REVIEW

2.1. Crystal chemistry of the clinopyroxenes

The pyroxene group is an important group of rock-forming minerals stable in both igneous and metamorphic rocks. They are found in a wide variety of rocks with compositional ranges from ultramafic (mantle rocks) to felsic (rhyolite). In their most basic form, pyroxenes have a generalised chemical formula of $M2M1T_2O_6$ and are classified as inosilicates consisting of single SiO_3 chains of linked SiO_4 tetrahedra (Nesse, 2000). The M cations of the octahedral layer can either be positioned in the M1 structural site (where cations lie between the apices of the SiO_3 chain) or the M2 structural site (where cations lie between their bases) (Deer *et al.*, 1997).

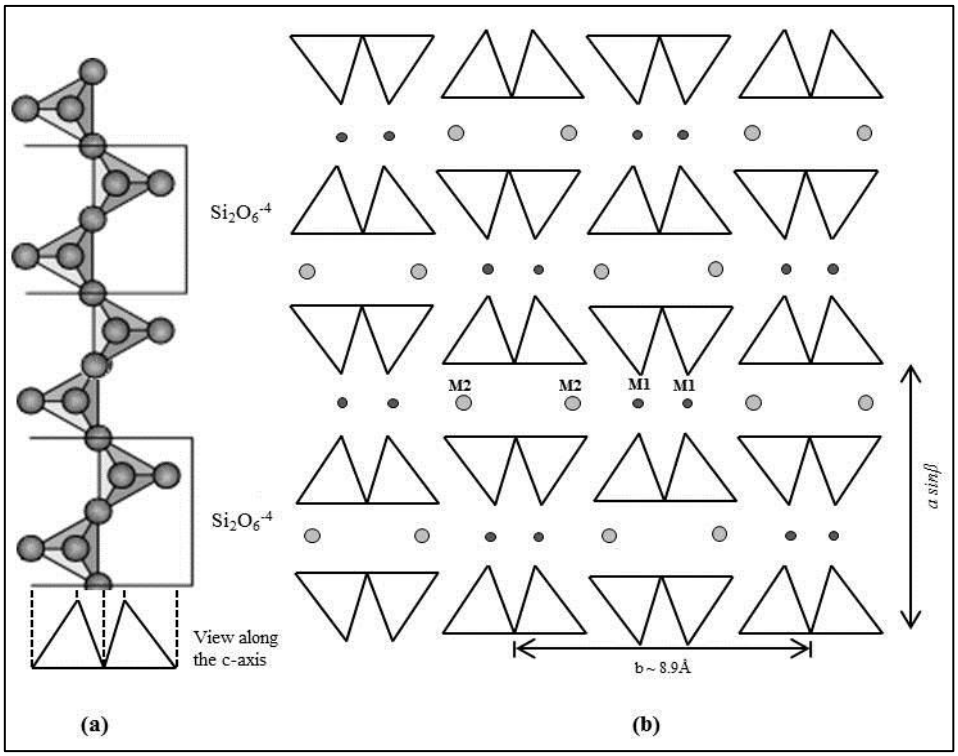

Figure 2. 1: An ideal pyroxene chain. It forms a single chain with the M1 and M2 cations creating edge-sharing octahedral chains between the peaks of the tetrahedra and the bases of the tetrahedral respectively (Putnis, 1992).

The M2 structural site refers to cations with an irregularly shaped octahedral coordination. It is occupied by cations that are positioned at the base of the tetrahedra in a 6-

fold coordination for Mg or 8- fold for Ca and Na coordination (Morimito *et al.*, 1988). This site may also be filled with Na^{+}, Fe^{2+}, Mn^{2+}, Mg^{2+} and Li^{+} to sum to 1.00. The M1 structural site consists of cations with a steady octahedral coordination (Deer *et al.*, 1997). This 6-fold structural site lies between oxygen peaks of the adjoining chains (Morimoto *et al.*, 1988). It is reserved for Al^{3+} and Fe^{3+} which is in excess of the T site with the addition of Ti^{4+}, Cr^{3+}, V^{3+}, Ti^{3+}, Zr^{4+}, Sc^{2+}, Mg^{2+}, Fe^{2+} and Mn^{2+} until it can be summed up to 1.00 (Morimoto *et al.*, 1988). The T structural site refers to cations in a tetrahedral coordination and is filled by Si^{4+} with Al^{3+} and Fe^{3+} in some rare cases (Morimoto *et al.*, 1988).

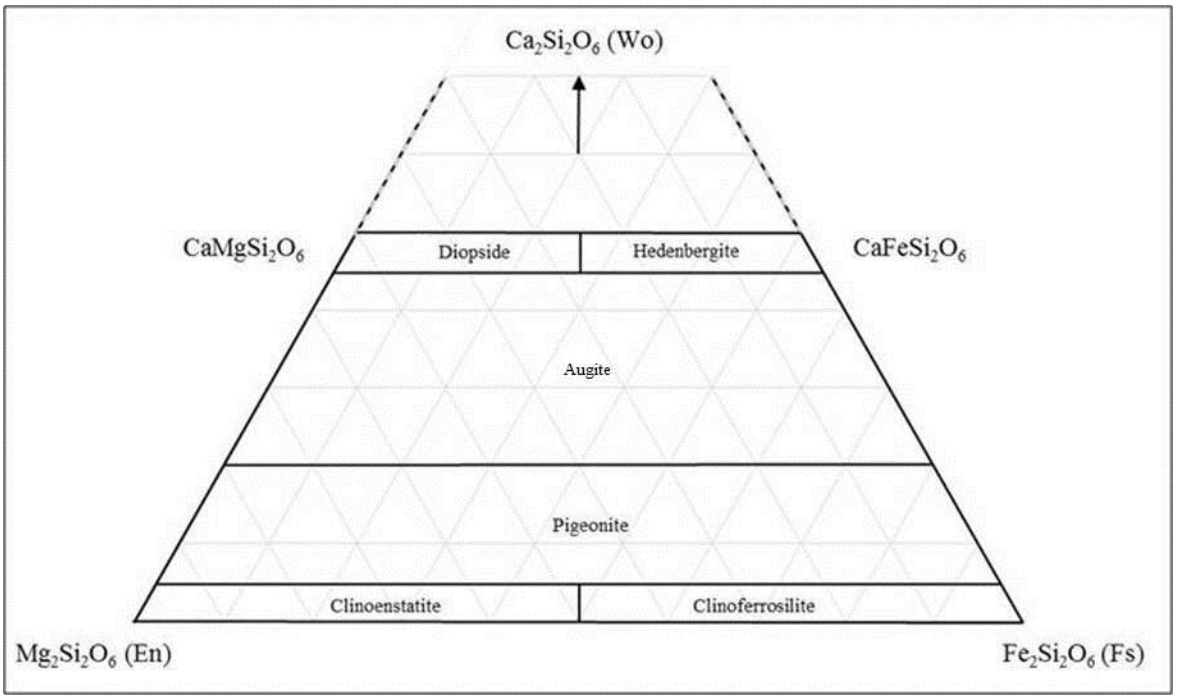

Figure 2. 2: A ternary diagram showing the pyroxene classification diagram and their compositional ranges and accepted names (Morimoto *et al.*, 1988). The major end-members are enstatite (magnesian end-member), ferrosilite (iron end-member) together with wollastonite at the apex. However, it is uncommon to find a pyroxene with a $CaSiO_3$ content more than 50%. Thus, a quadrilateral classification scheme is used.

The pyroxene structure is made up of alternating I-beam unit structures. This is important in determining whether a pyroxene has an orthorhombic or monoclinic crystal system (Morimoto *et al.*, 1988). Its monoclinic form, commonly referred to as clinopyroxene subgroup, is made up of I-beam structures with M1 octahedron in (+) orientation and also lying in the same direction along the (001) view. Clinopyroxenes contain a bit more Ca than orthopyroxene, where Ca makes up more than two-thirds of the M2 site. It is important to

note that the M1 void is smaller than the M2 site. The M1 site is positioned at the apices of the chains and filled with Mg and Fe (Nesse, 2000). The M1 octahedra together with the silicate tetrahedra share the apical oxygen atoms. The tetrahedral chain above the M1 site tends to be offset and also has the same effect on the M2 slabs, thus compensating and resulting in a monoclinic unit cell. The M2 void is larger and its shape is a lot more distorted. It can either form an octahedral when it contains a smaller cation or create 8-fold sites when occupied by a larger cation that is positioned between the bases of the tetrahedra (Putnis, 1992).

Complete solid solution occurs between the most common monoclinic pyroxenes. These form a four-component end-member system which consists of the following Ca-Fe-Mg pyroxenes: $CaMgSi_2O_6$- $CaFeSi2O_6$- $Mg_2Si_2O_6$- $Fe_2Si_2O_6$ (diopside-hedenbergite-enstatite-ferrosilite) (Figure 2.2). There are some occurrences through which Ca-rich clinopyroxenes may contain less Ca, more Mg or Fe in the M2 site in addition to the appreciable amount of Al in the M1 site. This compositional confine closely depicts an augite.

2.2. Review of clinopyroxene megacrysts from around the world

Irving (1974) evaluated over 150 clinopyroxene megacrysts from around the world and compared them to those collected from soils at Pliocene-Holocene basalt cones of the Newer Basalts province of Victoria and South Australia, and a few others from basaltic rocks of south-eastern Australia. Clinopyroxenes within this compilation are typified as vitreous in appearance and chemically homogeneous, with $Mg/Mg+Fe^{2+}$ ratios ranging between 75 and 90. This indicates that the crystals could have formed from primitive basalt which originated from a deep mantle source (Irving, 1974).

Minor inclusions of apatite, sulphides and spinels were also observed in megacrysts from Dish Hill, California (Binns *et al.*, 1970; White, 1966) and Besolles, France (Irving, 1974). Titaniferous spinels and Ni- and Cr- bearing iron sulphides of Victoria occur as spherical or ellipsoidal grains regularly distributed along curved planes within the clinopyroxene megacrysts (Irving, 1974). No apatite or olivine inclusions have been recognised in clinopyroxene megacrysts from the Newer Basalts. Spherical sulphide inclusions have also been identified within the augitic clinopyroxene megacrysts collected

from a spatter cone on Nunivak Island, Alaska. The clinopyroxene is compositionally zoned with sulphide inclusions being quite similar in composition to those reported by Irving (1974). Pyrrhotite is the predominant sulphide which also has significant amounts of Ni (Peterson and Francis, 1977).

The Central Massif can be used as a typical example of continental intraplate alkaline magmatism. It is made up of volcanic fields which are Tertiary-Holocene in age. Amongst all volcanoes reported at Central Massif, Mont Briancon is most relevant to this study. It is a 1.6 ±1 My old scoria cone which lies along the NW-SE trending Devès plateau (Lorand *et al.*, 2003). The rocks of this occurrence consist of a coarse aggregate of clinopyroxene and olivine. Most clinopyroxene megacrysts from this region are vesicular, rounded and can be up to 22.5 mm in size. Woodland and Jugo (2007) reported that the olivine in this aggregate has high forsteritic content with some minor Ni concentrations. The paper further endorse that this type of olivine is analogous to a mantle-derived olivine, and hence cannot have been derived from a peridotite source, but rather must have crystallised contemporaneously with the clinopyroxene. This paper concluded that the olivine-clinopyroxene aggregate must have crystallised at shallow mantle depths. Euhedral crystals of apatite and sphene have also been reported within some megacrysts (Woodland and Jugo, 2007).

The rare clinopyroxene megacryst aggregates from basalts of the Leizhou Peninsula, South China are also worth mentioning (Huang *et al.*, 2007). Volcanism within this region started in the late Oligocene and lasted till the Holocene period. They occurred due to rifting in an east-westerly direction leading to the opening of the South China Sea Basin (Ho *et al.*, 2000). Clinopyroxene megacrysts were collected at the Yinfengling volcanic breccia (Yu *et al.*, 2003). These megacrysts are unique in that garnet and orthopyroxene exsolves from clinopyroxene, forming lamellae, and thus can be used to reconstruct the thermal history in this region (Huang *et al.*, 2007). Huang *et al.* (2007) suggest that the exsolution of garnet-orthopyroxene is possibly due to the decrease in temperature conditions in the upper mantle, during the evolution from the spinel-pyroxenite field to the garnet-pyroxenite field. A garnet-orthopyroxene-spinel cluster can be found within a granular zone of the clinopyroxene megacryst and probably formed due to downwelling of the asthenosphere during the thermal decay of the lithosphere (Yu *et al.*, 2003).

2.3. Review of clinopyroxenes found along the Southwest Indian Ridge

Johnson *et al*. (1990) determined the evolution history of the oceanic lithosphere by studying the chemical features of abyssal peridotites with respect to key incompatible elements. The authors studied the mantle melting dynamics of discrete diopsides from residual abyssal peridotites from fracture zones cutting through the Southwest Indian Ridge systems, which extend from the Bouvet Island to the Central Indian Ocean. This separates the African plate to the north from the Antarctic plate to the south. Bouvet Island and Marion Island both serve as surface expressions of hotspot volcanism rising upon a shallow seafloor. The clinopyroxenes exhibit some degree of orthopyroxene exsolutions. In the study, the authors concluded that abyssal peridotites sampled near the Marion hotspot have greater degrees of melting in the upper mantle and this is manifested in peridotites clinopyroxene compositions in which, the abundances of incompatible trace elements form a steeply sloping light to medium REE depleted patterns.

2.4. Marion Island clinopyroxene megacrysts

Marion Island clinopyroxene megacrysts were handpicked from a scoria cone, named Pyroxene Hill, located in the southern region of the island (Figure 2.3). The megacrysts occur as isolated, near perfect euhedral crystal with sizes ranging between 3 mm and 5 cm (Figure 2.4). Most of the megacrysts are black to deep green in colour with a glassy lustre and polyhedral, equant habit. The majority of crystals appear to be symmetrical with macroscopically smooth surfaces. A few of the crystals are slightly weathered, rough with rounded margins and cavities possibly due to fracturing and melt reacting with the crystals en route to the surface. Some areas on the surfaces are slightly tinted (brown), possibly residual material from the scoria. A total of 18 crystals were chosen from 3 kg worth of material from the scoria cone to make up the sample suite of this study. The least weathered and most euhedral crystals were selected to make up the sample suite.

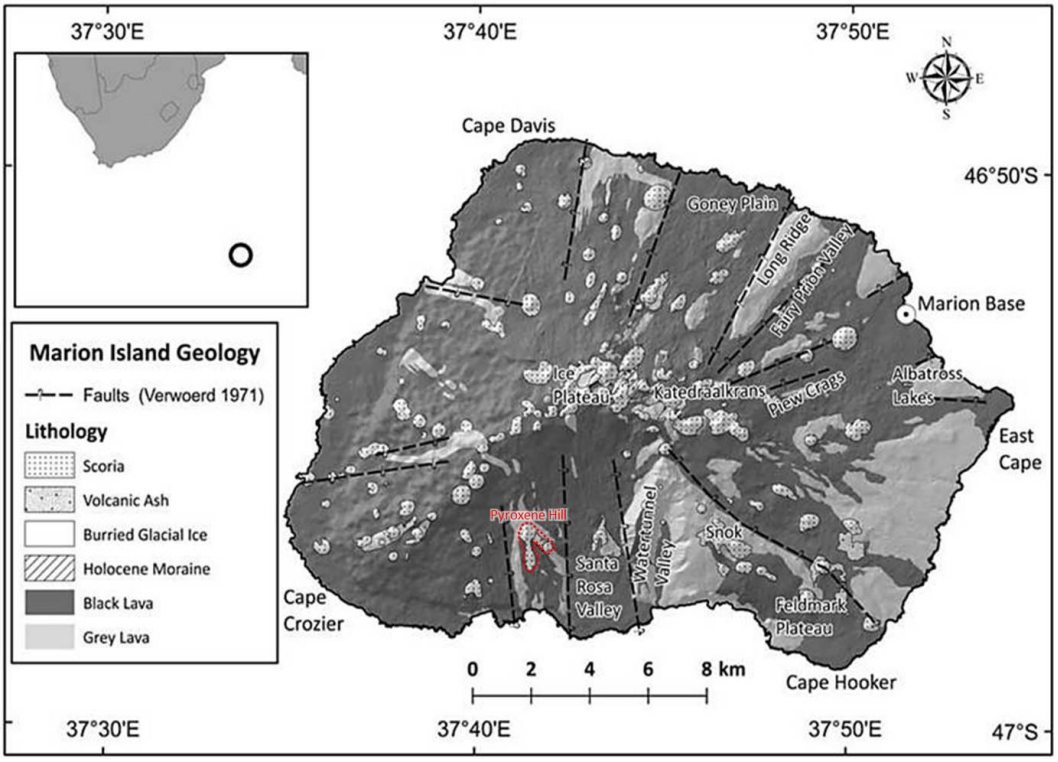

Figure 2. 3: A simplified geological map of Marion Island showing the sampling locality, Pyroxene Hill (circled in red) (Hall *et al.*, 2011).

Previous work conducted on the clinopyroxene samples used in this study distinguished that there is complex zoning in the clinopyroxene megacrysts. The Marion clinopyroxenes show irregular zoning patterns. Three compositional zones were identified within the crystals, based on clinopyroxene chemistry. The first type of zone represents clinopyroxenes that may have formed from the most primitive liquid. The other two groups are the most dominant type of clinopyroxene and crystallised from a slightly more evolved liquid (Botha, 2013).

Figure 2. 4: An image showing clinopyroxene megacrysts (dark green crystals) and red scoria samples (reddish-brown rocks) randomly picked on Pyroxene Hill. The most euhedral and least weathered clinopyroxene crystals were selected to make up the sample suite (Botha, 2013).

This variation in composition suggests that the megacrysts may have crystallised at different levels prior to ascent. The three growth stages are clearly depicted in Cr_2O_3 vs. TiO_2 vs. Al_2O_3 diagrams (Figure 2.5). According to Krause *et al.*, (2007), more primitive magma would contain higher concentrations of Cr_2O_3 and lower concentrations of TiO_2. As the liquid starts to crystallise, the Cr in the liquid will be incorporated into the crystal structure. Relative to the Cr_2O_3 concentration of the liquid, the TiO_2 concentration will increase. The majority of the microprobe results plot in the lower Cr_2O_3 and higher TiO_2 range, thus implying that the majority of the crystal growth occurred in a slightly more evolved liquid rather than a purely primitive mantle melt.

The Nimis and Taylor (2000) geobarometer was used to determine a possible crystallisation pressure based on the partitioning of Cr and Al in the clinopyroxene crystal lattice. This produced a pressure range of about 15 and 25 kbar which corresponds to depths of about 50 to 75km (Figure 2.5). However, the reliability of the barometry results is

questionable as the calculations made no reference to the Fe^{3+} content of the samples, which is present in large amounts.

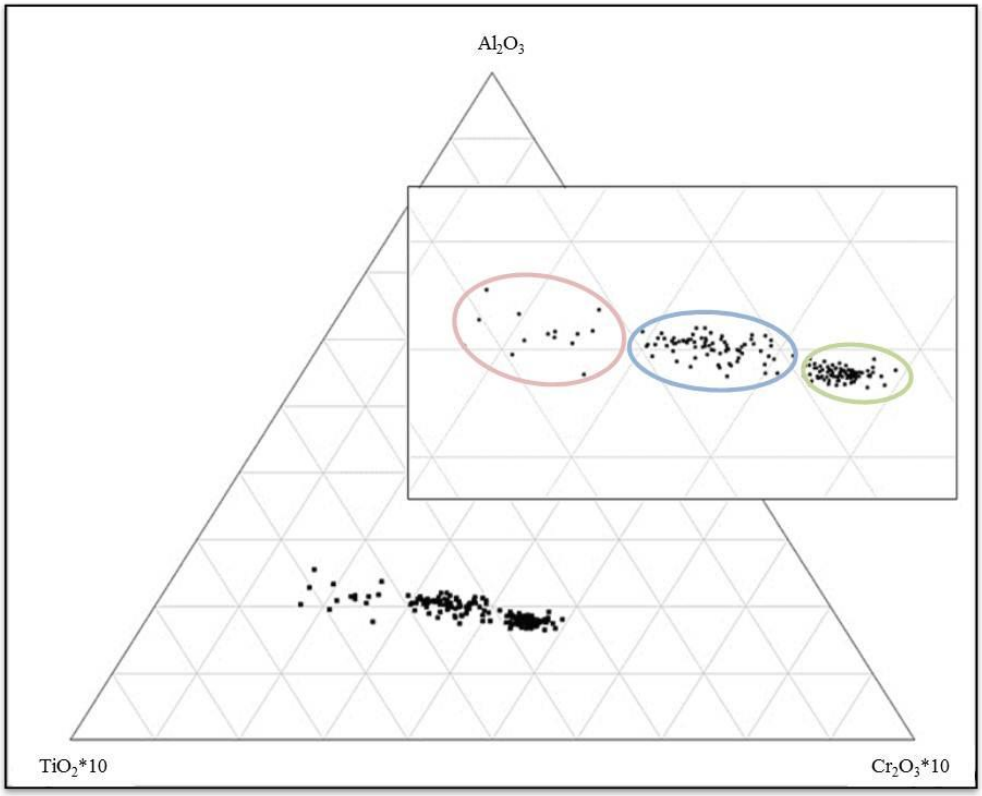

Figure 2. 5: Al_2O_3, TiO_2 and Cr_2O_3 ternary diagram of clinopyroxene data taken from line analysis using an electron microprobe. This shows variation in composition within a single clinopyroxene megacryst and this data shows three distinct compositional classes (Botha, 2013).

2.5. Review of the selected characterisation techniques used for the analysis of the Marion Island clinopyroxene megacrysts

2.5.1. Tomography

X-ray computed tomography (CT) is a rapidly developing technology which has proven to add value to the earth sciences in recent years. Formerly developed for the medical field (in the early 1970s), this technology serves as a reconstructive and imaging application for soft tissue and bones (Ketcham and Carlson, 2001). X-ray CT is a quick and non-destructive method that is easily adaptable in the geologic field of study, aimed at producing successive and adjoining slices through samples and merging them to create finely detailed images that are a true representation of the studied samples. This process involves generating 3D and 2D images that can be used to study the porosity and permeability of sediments,

metamorphic textures, fluid flow dynamics, meteoritic as well as mammalian skulls in the paleontological field (Mees *et al.*, 2003). This method has made the acquisition of qualitative and quantitative geological data easy with an added benefit of completing the analysis without obliterating valuable samples that can never be replaced. A disadvantage of the novel medical CT is that the resolution is too low for conducting a detailed scan of geologic materials. This limitation has been circumvented through the development of a microfocus CT (µCT) which employs the same principles used in a medical CT but provides a superior resolution which can be as low as 10µm x 10µm x10µm (Van Geet *et al.*, 2000).

X-ray CT can be defined as a non-destructive imaging technique which enables the user to visualise the internal structures within non-translucent objects (Van Geet *et al.*, 2000). Some of the most fundamental elements of tomography are the X-ray source, the object through which the X-rays pass through, and detectors which measure the degree of X-ray attenuation within the objects (Ketcham and Carlson, 2001). An essential principle in tomography is to obtain a consecutive series of X-ray images and views (refers to the intensity measurements on all detectors for a given object position and scanner geometry) of the object over numerous angles of orientation taken from 0-360 degrees around the object. The resulting dimensional data is then used to create 2D slices through the object and resembles what one would see if one were to slice the sample along the scan plane (Ketcham and Carlson, 2001). However, this is highly reliant on the degree of X-ray attenuation within the objects (Van Geet *et al.*, 2000).

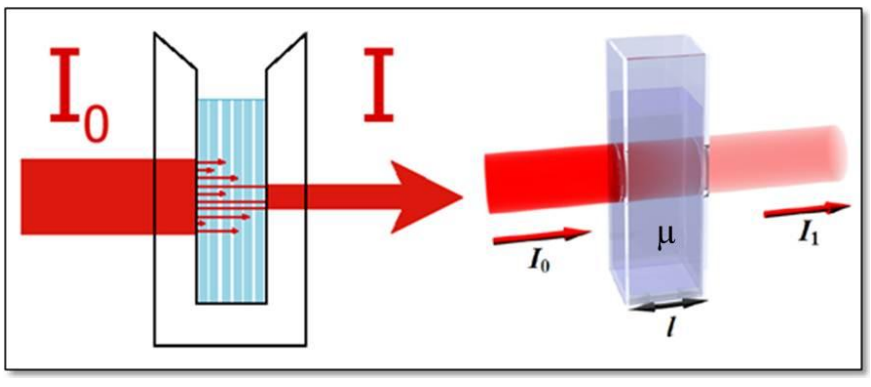

Figure 2. 6: Image shows how Beer-Lambert's 3rd law of optics can be applied to an object. It shows that an X-ray intensity passing through a sample with varying degrees of absorbency will decrease exponentially with length as it passes through the sample, l (Kimia, 2011). Consequently, the resultant x-ray intensity, I, will be much lower than the initial x-ray intensity, I_o.

The Beer- Lambert Law of optics can be used to explain the interaction of X-rays with an object (Figure 2.6). This is a law that governs the absorption capacity of a material when a mono-energetic beam of X-rays passes through homogenous materials. In principle, the law asserts that the intensity of an X-ray passing through a material with wavelength, I will drop exponentially with l,

$$I = I_0 \, exp \, [-\mu l] \, , \qquad (1)$$

Where I_0 is the initial X-ray intensity, μ is the linear attenuation coefficient of the scanned material, and l is the length of the x-ray path through the material.

Most rock samples consist of more than one mineral thus the formula in this instance will become:

$$I = I_0 \, exp \, [\sum_i (-\mu_i l_i)] \, , \qquad (2)$$

with each occurrence of an additional mineral phase being represented by i. Most CTs used currently are operated at X-ray energies ranging between 30 and 200 keV. This means that coherent scattering, Compton and photoelectric effects will occur. The linear attenuation coefficient (μ) for the above-mentioned energy field relies upon both the mass density (ρ) of the material as well as its effective atomic number Z_{ef}. The relationship between all three variables is represented by the formula below:

$$\mu = 5\rho N_A 10^{-28} \left\{ 0.597 \exp[-0.028(E-30)] + 1.25 \frac{Z_{ef}^{2.0}}{E^{1.9}} + 9.8 \frac{Z_{ef}^{3.8}}{E^{3.2}} \right\} , \qquad (3)$$

Where N_A is Avogadro's constant; E is the x-ray energy (keV); and Z_{ef} is the effective atomic number of the sample which can be calculated by summing up the electron concentration of the i^{th} component of the sample. The first variable within the brackets represents the Compton Effect, whilst the second and third variables represent the coherent scattering and photoelectric effect respectively.

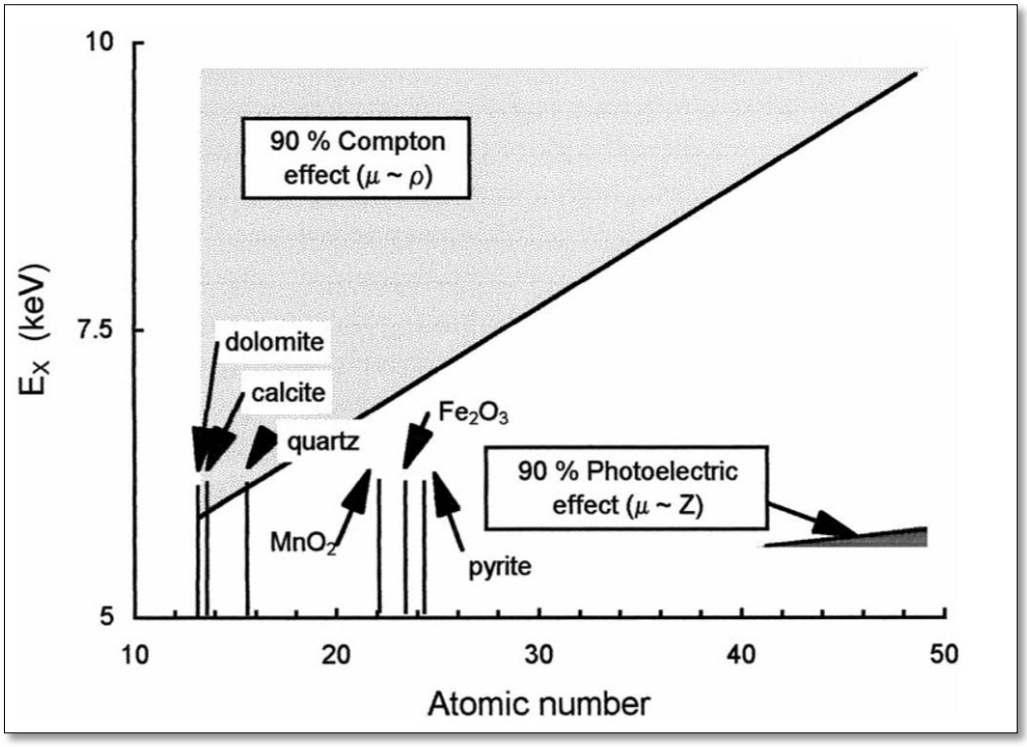

Figure 2. 7: The graph illustrates the rationing relationship between the Compton and photoelectric effects. The upper region of the curve reflects that the Compton Effect is the dominant attenuation mechanism whilst at lower energies the photoelectric effect is more dominant, thus sensitive enough to distinguish between various minerals. (Duliu, 1999).

Geological samples are preferably scanned at X-ray energies less than 100 keV, thus resulting in the photoelectric effect becoming a notably crucial attenuation mechanism. This is supported by the veracity that photoelectric absorption is proportional to Z^{4-5} (where Z is the atomic number of the attenuating material), thus making low X-ray energies more sensitive to differences in composition in relation to those at higher energies (Figure 4.2). The Compton scattering is dominant for higher energy sources of up to 10MeV and with μ being proportional density (ρ) of the sample only (Markowics, 1993).

2.5.2. Scanning electron microscopy

Scanning electron microscopy (SEM) is an analytical technique often used to gather the morphological characteristics of a sample. This includes sample texture, the chemical composition of minerals, its crystalline structure and orientation (Swapp, 2012). SEM uses electrons for imaging at substantially high magnification and focus depths (Goldstein *et al.*, 2012). A sample is typically bombarded with a focussed electron beam (consists of electrons produced at the top of the column and passed through a combination of lenses and apertures)

with energies of up to 40 kV. The secondary and backscatter electron emissions from the analysed surface are of great importance when using this technique. These often vary according to differences in surface topography and composition (Goldstein *et al*., 2012). The emitted secondary electrons are then used to form micrographs of the targeted surface (Bogner *et al*., 2007).

It is the quickest way of identifying the inclusions present even at resolutions of less than 1 nm within the megacrysts. This is dependent on the analytical and instrument settings of the SEM (Müssig, 2010). A scanning mode which generates a 2-D image, high-resolution images may be selected in order to show the spatial variation in chemical composition of minerals present in a sample. Energy dispersive X-ray spectroscopy (EDS) may be coupled with a SEM and is used to acquire element maps and to determine the chemical composition of minerals by performing a semi-quantitative analysis for a selected number of points. This technique requires minimal sample preparation and the acquisition is fast.

2.5.3. Electron Probe Microanalysis

Electron Probe Microanalysis (EPMA), which is informally known as an electron microprobe, is a routine quantitative and non-destructive method for performing precise elemental analysis of mineral species with elements from boron to uranium. This analysis is performed on surface materials commonly mounted on thin sections or briquettes to qualitatively identify and to quantify the composition of the mineral of interest at micrometer (µm) and nanometer (nm) scale (Goldstein *et al.*, 2012). This technique is non-destructive, easy to use and it is relatively simple to interpret the results. This information is crucial in determining if there are any chemical variations within the analysed mineral. EPMA instruments are also fitted with imaging detectors such as SEI, BSE and miniCL, which permit simultaneous X-ray (WDS and EDS), SEM and BSE imaging. This technique is quite similar to SEM but provides far better results as it is more sensitive when analysing light elements and it also limits the risk of erroneous interpretation of qualitative spectra by using mineral standards.

2.5.4. Raman Spectroscopy

Raman spectroscopy is a powerful vibrational spectroscopic technique commonly used to rapidly identify and to characterise various minerals ranging from iron-bearing mineral phases to rare minerals (Griffith, 1969). Scattered light from the Raman spectrometer is used to examine molecular vibrations which are crucial in determining the structural properties of the observed mineral phase. This is also important when inspecting crystal symmetry, electronic environment and molecular bonds (Willard *et al*., 1986). The phenomena of inelastic scattering effect, commonly referred to as the 'Raman Effect', refers to the minute change or shift in wavelength as radiation is scattered by a molecule and known to have a frequency dissimilar to that of the incident beam (Raman & Krishnan, 1928). This shift in wavelength is controlled by the chemical structure of the molecules inducing the scattering process (Willard *et al*., 1986). According to Kaur (2006), inelastic light scattering results in the excitation and the deactivation of molecular vibrations in which either the photon may lose or gain some amount of energy, thus giving root to a shift in photon frequency.

Raman spectroscopic studies provide detailed chemical and structural details of solid phases through the identification of a mineral's crystallographic plane. Raman spectroscopy can also be used in determining the local molecular structure with high spectral resolution (Hanesch, 2009). It provides basic information on mineral symmetry, elemental speciation and crystallinity estimates for the mineral of interest (Pasteris *et al*., 2001). There are also other techniques that can be used to gather this information or which have similar capabilities as the Raman. This technique stands out as the preferred technique because it is structure specific, quick and requires minimal sample preparation. What also makes it stand out is its ability to differentiate between different oxidation states. These are identified as elements of concern often absorbed onto iron oxide phases.

CHAPTER 3 – ANALYTICAL SETTINGS

Several different analytical methods were used during this project to analyse the clinopyroxene megacrysts from Marion Island. Analytical parameters for each are given below.

3.1. Morphological analysis

3.1.1. Tomography

Thirteen of the least weathered megacrysts were obtained and scanned using a 225kV microfocus X-ray CT system from Nikon Metrology, based at NECSA in Phelindaba, South Africa. The X-ray source was operating at energies ranging between 60 and 100 keV and at currents of between 80,100 and 170 uA depending on the dimensions of the sample. A $0\text{-}180^0$ scanning interval was used on each megacryst with an acquisition time of about 30 minutes. Al was used as a filtering material. A minimum of 500 radiographs were collected for each sample. VGStudio MAX 2.2 software package (a high-end product by Volume Graphics) was used for the visualisation and analysis of data derived from the CT system. This is inclusive of the construction of 3-D and cross-sectional images which are merged to create videos.

3.2. Chemical analysis

3.2.1. Scanning Electron Microscopy (SEM)

SEM analysis was run using the JSM-8500 LV Scanning Microscope at the University of Pretoria, Physics Department on six clinopyroxene megacrysts on polished mounts. The EMITECH K950 coater was used to apply a thin film of carbon prior to analysis, to permit electron conductivity. The SEM's scanning mode was used to produce high-resolution images showing the spatial variation in chemical composition of the minerals present in the samples. A Thermo Scientific Noran System Seven (NSS) EDS was used to determine the chemical composition of the inclusions present by acquiring a semi-quantitative analysis for a selected number of points. Analytical conditions used included an accelerating voltage of 20kV, 1.100 live time and 40s dead time.

3.2.2. Electron Probe Microanalysis (EPMA)

Of the six polished mounts, five were selected for qualitative mineral analysis at Rhodes University using the JEOL JXA 8230 electron microprobe with the following analytical conditions: accelerating voltage of 15kV, a probe current of 20nA with 10s counting time on peaks and 5s for backgrounds on either side of the peak. The ZAF method was used for corrections. Before commencing with the analysis, samples were re-polished and coated with a thin film of carbon (~20nm thick) for electron conductivity. However, re-polishing resulted in the removal of some sulphide inclusions. Four samples yielded accurate quantitative analysis for the identified mineral phases, and also line analyses, elemental maps, and BSE images of inclusions within the clinopyroxene megacrysts were made.

3.2.3. Raman Spectroscopy

Raman spectra were obtained on some inclusions at *Ecole Normale Supérieure de Lyon*, using a multichannel Raman microprobe (LabRam HR800 from DILOR) equipped with a confocal microscope configuration that enhances the signal-to-noise ratio by eliminating most of the parasitic light from sample and diamond fluorescence. Experiments were conducted in a backscattering geometry with a Mitutoyo objective that focused the incident laser spot to less than 2 μm in diameter. The scattered Raman light was focused through a 100 mm slit into a spectrograph equipped with an 1800 gr/mm grating and analysed by a CCD detector, giving a resolution of approximately 2.5 cm^{-1} (Auzende *et al.*, 2004). The accumulation times for Raman spectra were typically 60–120 s over the spectral region from 100 to 1250 cm^{-1}. Precision on Raman peak position is typically 0.2 cm^{-1} (2s) for strong peaks; accuracy is 1 cm^{-1} with full-width at half maximum (FWHM) of about 0.5–1 cm^{-1}.

CHAPTER 4 – MORPHOLOGICAL ANALYSIS

Thirteen clinopyroxene (cpx) megacrysts were selected from the sample suite and scanned using a µCT (Figure 4.1). This application is the best approach as it provides means of examining the samples without destroying them. Porosity estimates, morphological and textural relationship of the associated minerals will be reported in this chapter. The megacrysts were arranged and analysed from smallest to largest based on sample diameter.

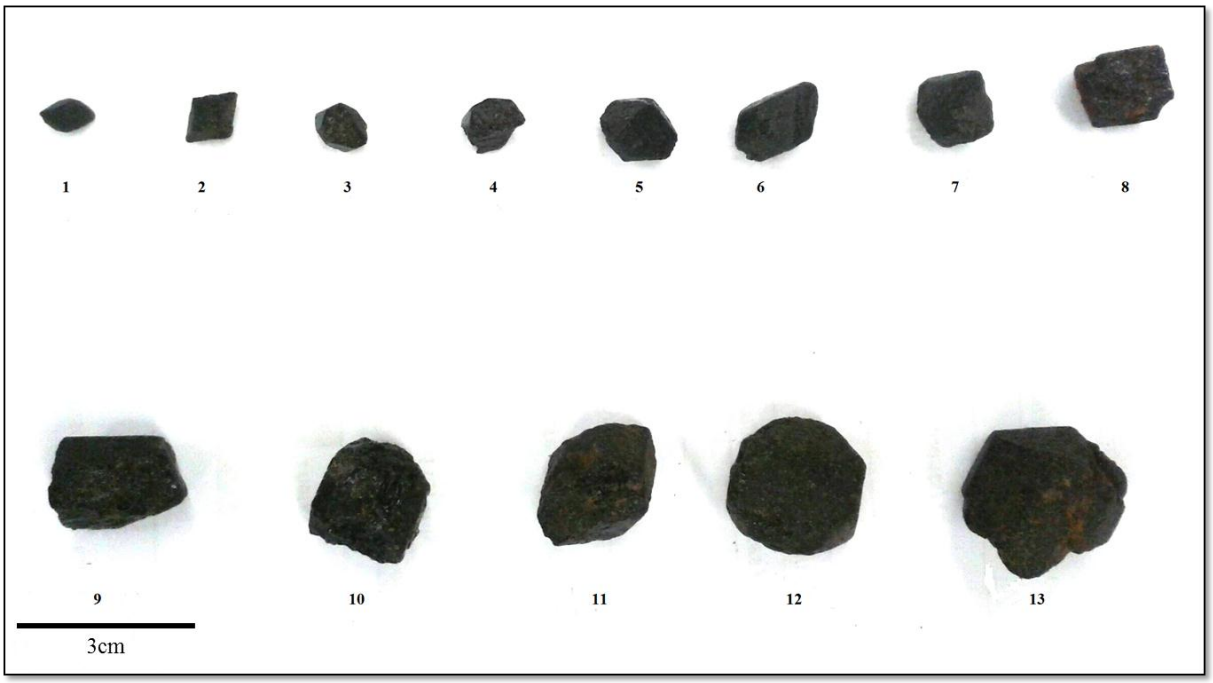

Figure 4. 1: Image showing 13 megacrysts which make up the sample suite. These were analysed using a 225kV microfocus X-ray/CT system at NECSA.

4.1. Importance of structure

Evaluating the internal and external morphological and textural properties of the megacrysts serves as one of the key elements in establishing the magmatic condition necessary for the growth and evolution of all mineral occurrences within the megacrysts. This provides compelling evidence on any adjustments to the environmental conditions or chemical composition having a considerable effect on both the growth rate and nucleation rate of the crystals (Corrigon, 1982). These chemical and environmental forces serve as motivating factors of magma solidification and are primary controls on both the textures and the compositional evolution of coexisting minerals and liquids (Welsch *et al*., 2016).

4.2. Implications of findings

Some researchers argue that the near-perfect morphology, size of the crystals and subtle compositional variation may possibly indicate that the megacrysts grew at conditions of low supersaturation over long residence times and that crystallisation took place at a somewhat shallow subvolcanic magma reservoir prior to magma ascent to the surface (Stearns and Macdonald, 1942). Others researchers have further interpreted their occurrence as crystallisation products of the associated host rocks produced at high pressure and temperature conditions, and in other cases occurring as disaggregated xenoliths of an exotic origin entrapped in the effluent magma (Binns *et al*., 1970; Green and Ringwood, 1967; Schulze, 1987). This is critical when making a judgement on the degree of supersaturation. Contrary to normal belief, high levels of supersaturation should be associated with large crystals of cpx and olivine. Moreover, low levels of supersaturation should represent syn-eruptive crystal growth (Welsch *et al*., 2016).

4.3. Porosity estimates

Porosity, which is defined as a measure of void spaces in a sample, is calculated from CT images by detecting pore spaces in a single scan by image segmentation techniques (Taud *et al*., 2005). The pore spaces are then extracted in accordance with the given scale corresponding to the CT image resolution and expressed as a percentage which may vary between 0 and 100% (Prokop *et al*., 2009). Segmentation is the first treatment applied to the images prior to analysis of the physical properties of the sample. It is used to set the dimensions of pore spaces and varies from micron to centimetre scale. Pore size and pore distribution estimates were made by highlighting the pore spaces with NIS elements (Figures 4.2B and 4.2C). This is commonly referred to as the grey level method (Taud *et al*., 2005). The porosity estimation results are reported in Table 4.1. The reconstructed images revealed that the megacrysts are highly porous with the majority of pore spaces concentrated at the core of each crystal (Figure 4.2B). The crystals are highly fractured, featuring a network of minute veins which are, in some instances, interconnected to the pore spaces (Figure 4.2C).

Determining the sample's pore estimates serves as quick indicator on the cooling conditions of the volcanic environment. It also reflects that the magma from which the cpx

megacryst formed had high volatile content and volatile saturation. This further suggests that reservoir pressurization led to the eruption incurred on Pyroxene Hill.

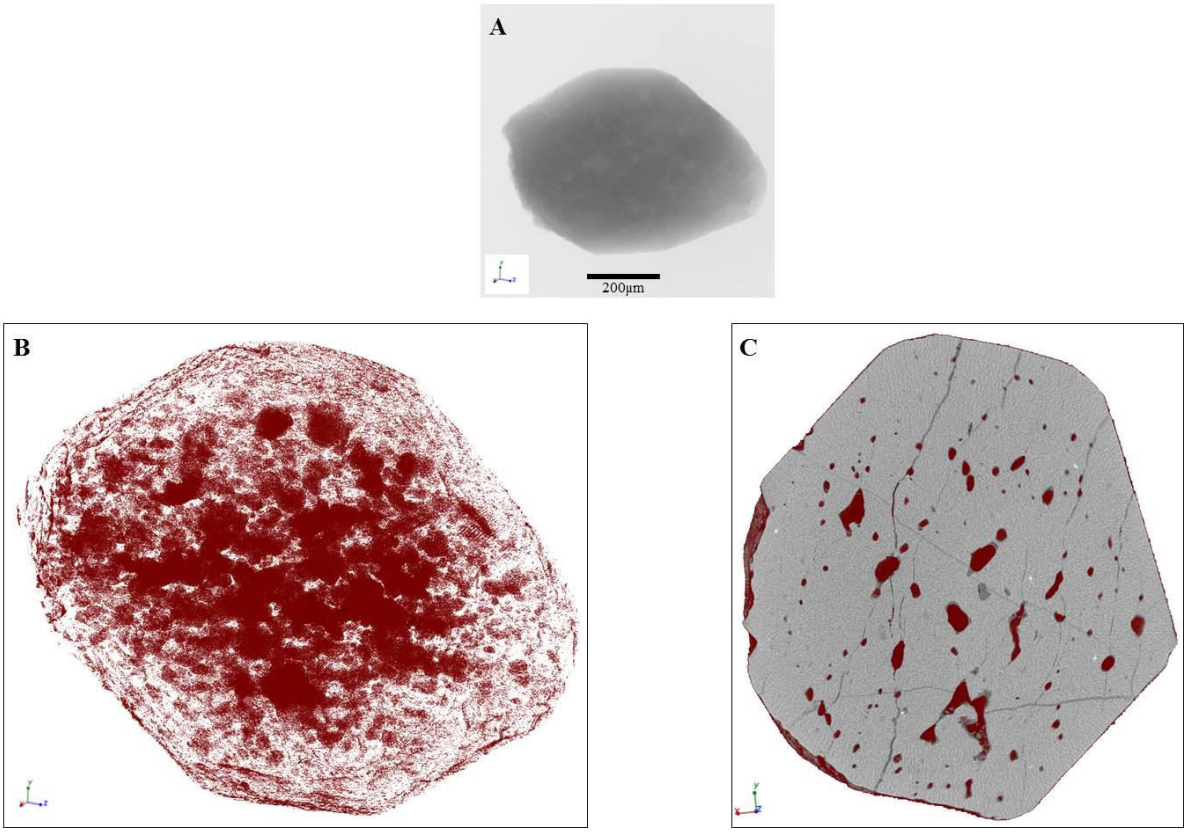

Figure 4. 2: Images showing the distribution of pore spaces within the megacrysts. (A) An X-ray shadow image. Most of the porous spaces occur at the centre of the megacrysts (B) and are interconnected with each other by fractures (C).

Table 4. 1: Porosity estimation by grey level method for selected clinopyroxene megacrysts.

Sample number	Total volume including background (mm^3)	Boundary or sample size(mm^3)	Porosity (mm^3)	Porosity(%)
2	154.39	151.03	3.36	2.18
3	177.88	169.04	8.84	4.97
4	282.98	264.50	18.48	6.53
5	528.08	473.37	54.71	10.36
6	890.56	835.32	55.24	6.20
8	1038.86	1021.30	17.56	1.69
13	4439.45	4086.98	352.47	7.94

4.4. Minerals present based on grey values

At first glance at the µCT images, four different mineral phases can be identified based on differences in grey values. This discrimination is generally a reflection of the degree of attenuation of the object as well as differences in mass densities (Figure 4.3). Minerals with higher mass densities such as metallic minerals and sulphides often have high grey values (bright white) whilst those with lower densities (e.g. silicate minerals) have low grey values (shades of grey to black). Different minerals attenuate at different x-ray energies; however, overlaps may occur due to minerals having similar mass densities as an example; hematite and magnetite have densities of 5.25 g/cm^3 and 5.20 g/cm^3 respectively.

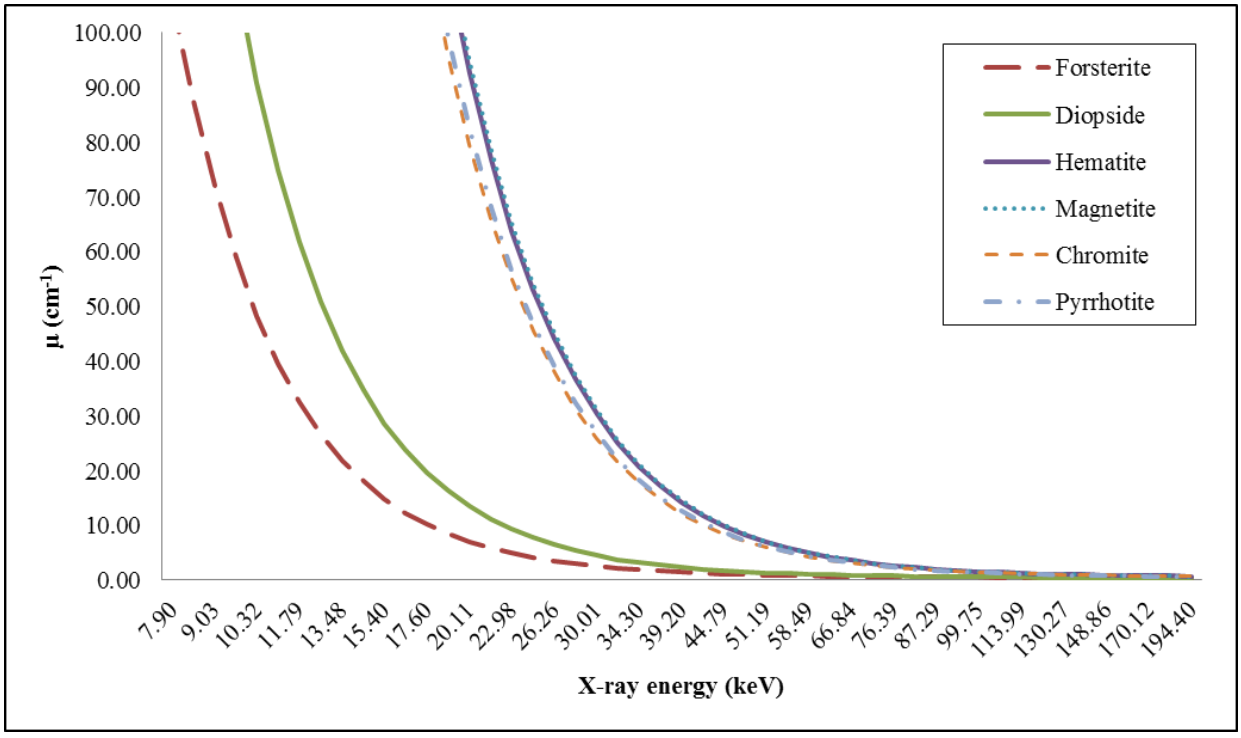

Figure 4. 3: The graph shows the linear attenuation coefficient plotted against x-ray energy for some of the common minerals present within the Marion Island clinopyroxene megacrysts. Curves for the silicate minerals (forsterite and diopside), hematite and magnetite curves overlap because they have similar mass densities (5.25 g/cm^3 and 5.20 g/cm^3 respectively), suggesting that difficulties may arise when trying to differentiate these two minerals. The attenuation coefficients converge making the minerals indistinguishable from each other, thus for geologic sample the energy window should strictly be at energies less than 100keV.

4.4.1. Phase relations of clinopyroxenes in CT images

A gradational change in grey value of the cpx megacryst has been observed in several of the studied megacrysts (Figure 4.4A). A transect drawn within the megacryst using an

µCT shows that some regions have higher grey values than others (Figure 4.4A) with the lighter patches being associated with higher grey values and the darker regions corresponding with lower grey values (Figure 4.4B). This reflects that these are two different mineral phases and also indicates that these minerals have chemical compositions which vary significantly possibly due to melt crystallising within fissures of a skeletal crystal, during magma cooling.

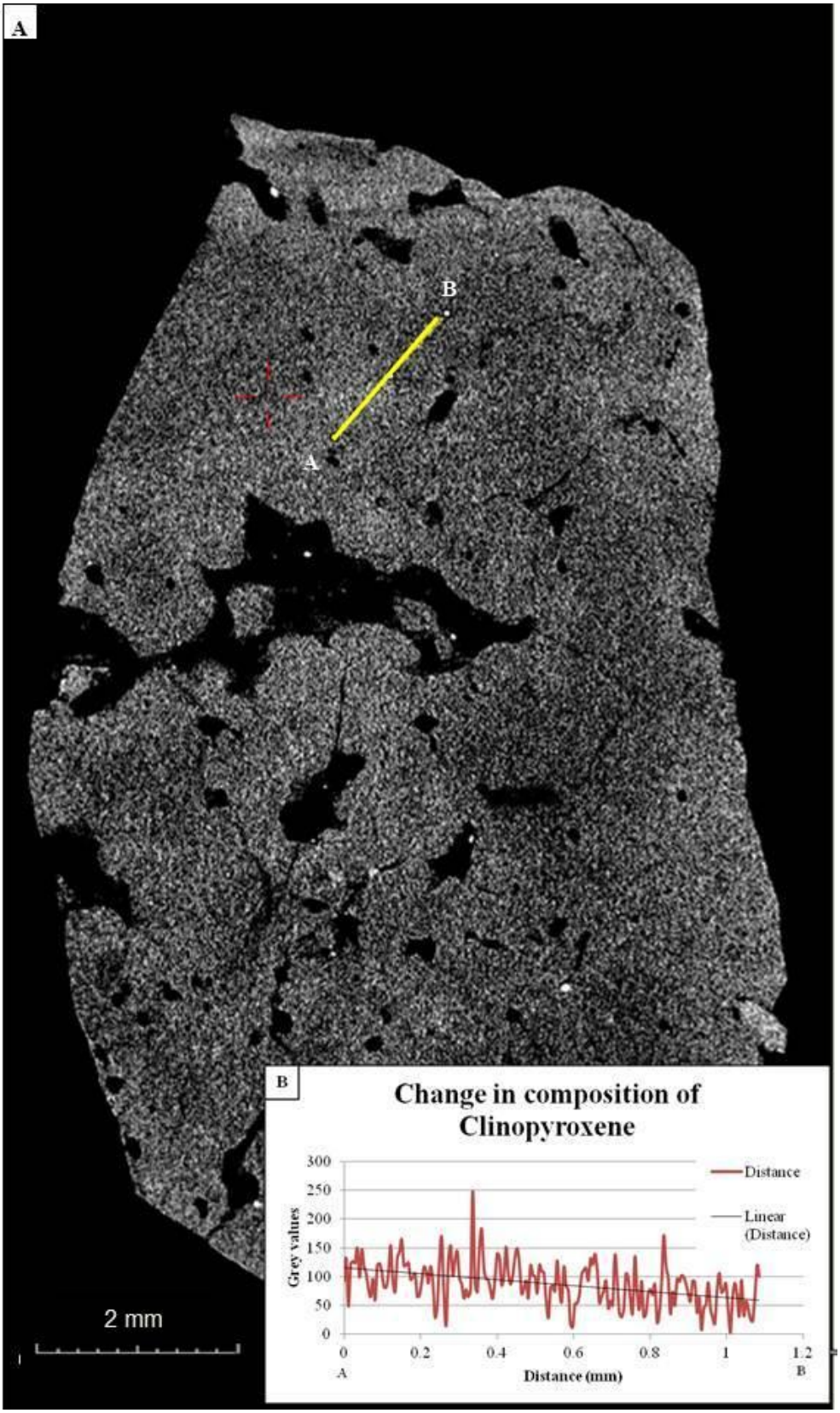

Figure 4. 4: A line profile taken using XRCT which involves the collection of various X-rays during the rotation of a rock sample (A). This profile shows variation in composition with reference to grey values. There is a decrease in grey values from point A to point B with the darker regions and lighter regions being associated with low (lighter material) and high grey (denser material) values respectively (B).

4.4.2. Phase relations of olivine in CT images

Euhedral to subhedral crystals of olivine (olv) were found within pore spaces of the cpx megacrysts (Figure 4.5 and Figure 4.7). Subrounded to well rounded olv crystals have also been identified and in some instances coexist together with the more euhedral olv crystals within a single cpx megacryst (Figure 4.5B). Olv makes up less than 6% of the total volume of the megacryst and is characterised by an orthorhombic crystal system and significantly high grey values when compared to those attenuated by the cpx megacryst. However, the somewhat rounded olv appears to have higher grey values than usual (Figure 4.6). This observation can only be explained as an effect of other minerals exsolving along cleavage planes of olv. Averaging out the attenuation coefficients of the two mineral phases leads to the olv attaining higher grey values.

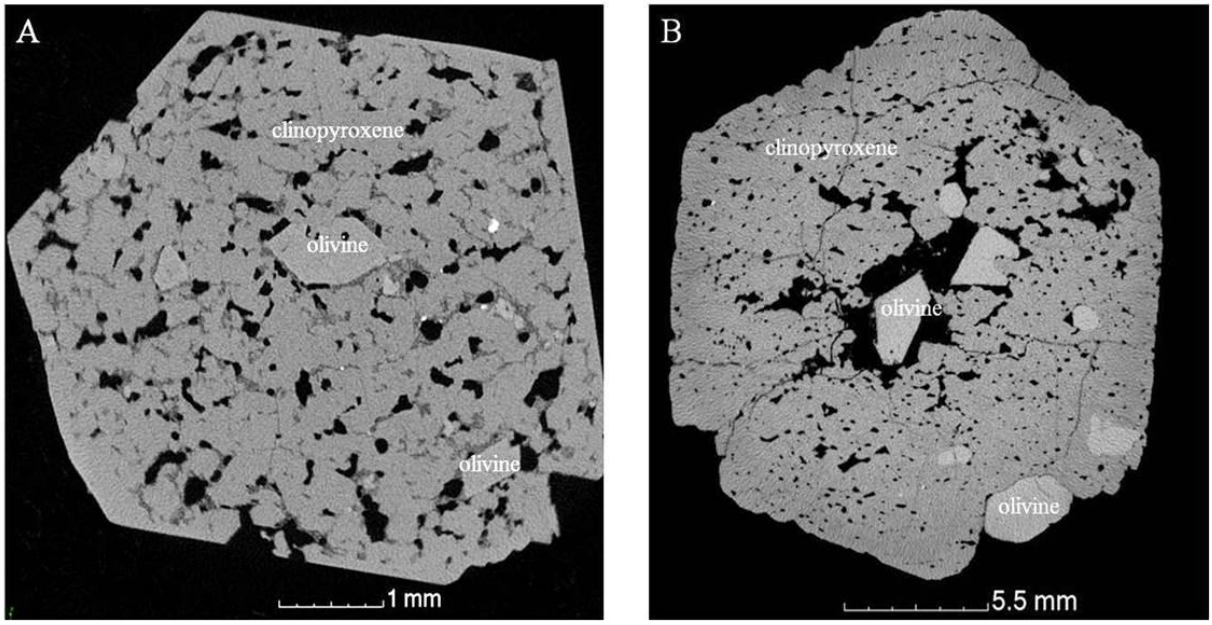

Figure 4. 5: Images showing euhedral to subhedral crystals of olivine included within the clinopyroxenes megacryst. In Figure (A), olivine displays low grey values while in other instances olivine has high grey values (Figure B). This reflects that hematite exsolutions (high grey values) are found in some of the olivine whilst some may lack this mineral phase.

4.4.3. Ancillary phases (Oxides and sulphides)

There are minor occurrences of minerals attaining the highest grey values (corresponding to a bright white colour). This high grey value reflects that the mineral has the highest density in comparison to the other mineral phases present within the samples. The

identified ancillary minerals are present as either discrete euhedral crystals or blebs within the megacryst, or as minute precipitates in the somewhat rounded olv (Figure 4.6). These minerals account for about 2% the total volume of the megacrysts and also have crystal diameters which are less than 0.2mm.

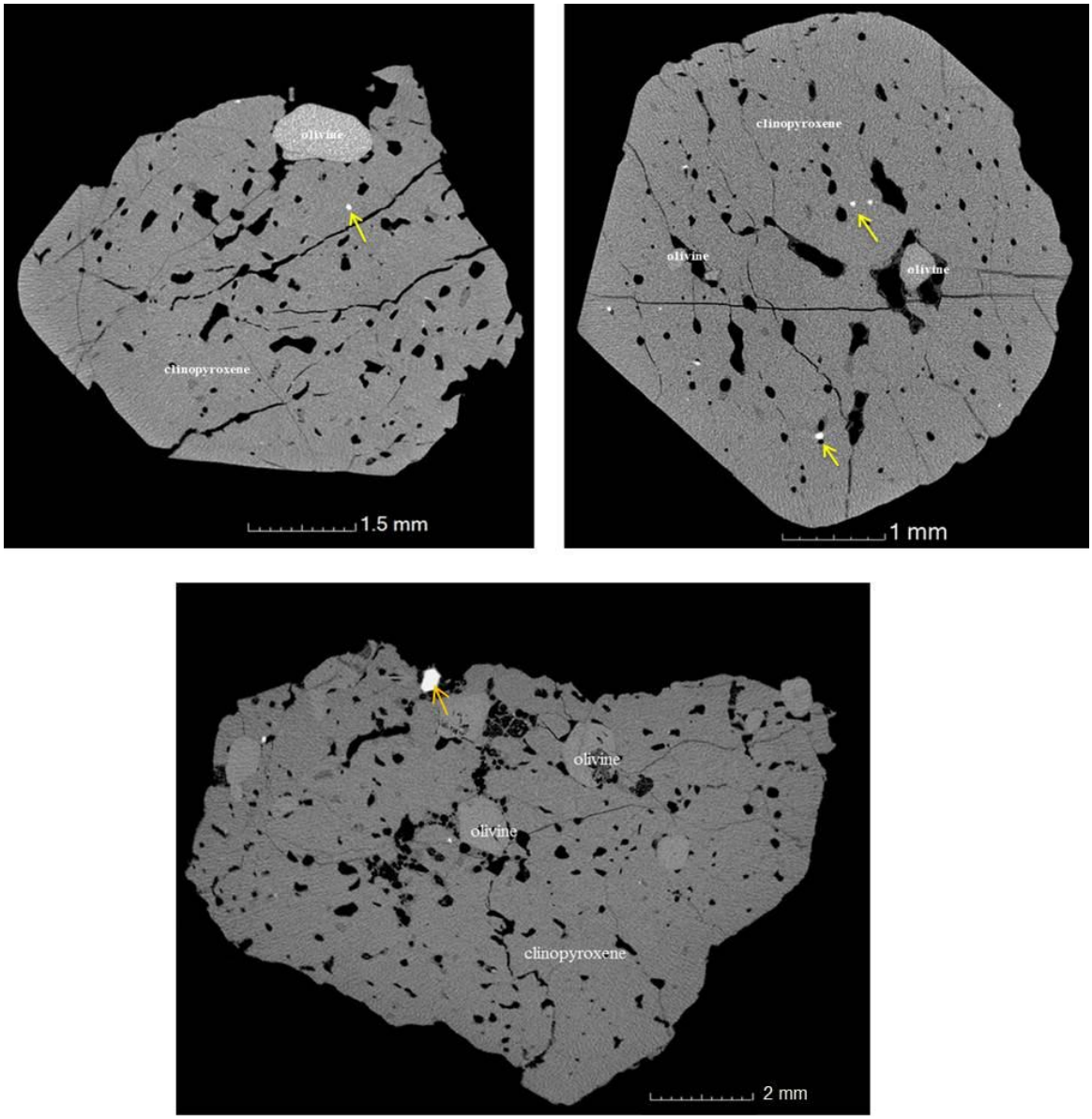

Figure 4. 6: Sulphide and oxide inclusions can be identified within the clinopyroxene matrices (yellow arrows). These obtained the highest grey attenuation values (bright white). The sulphides and oxides are easily distinguishable from each other as the sulphides often form blebs whilst the oxides are larger and occur as euhedral crystals.

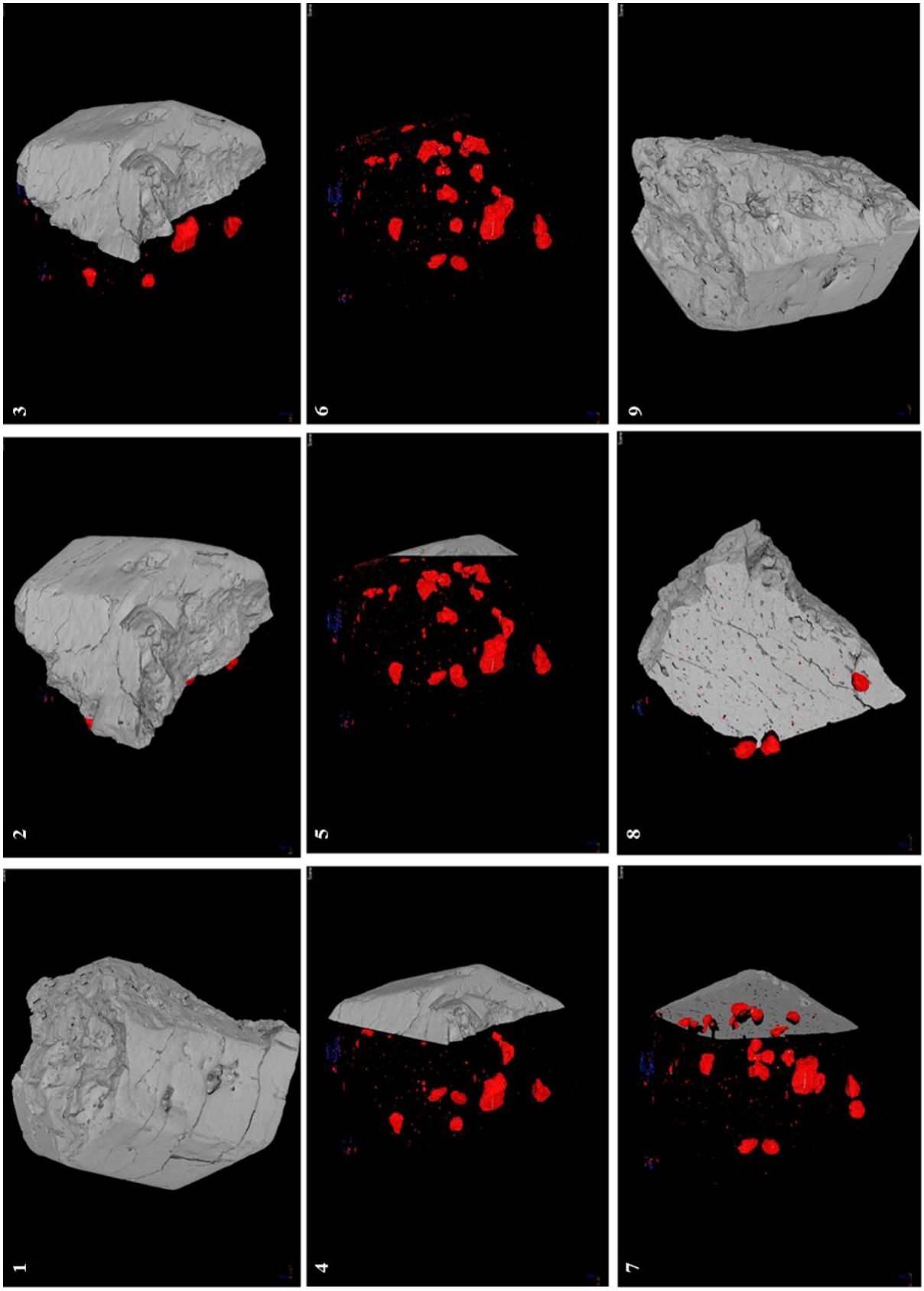

Figure 4. 7: Scenes from a movie created by loading slices of the megacryst taken using a µCT. The images were processed using VGStudio MAX 2.2 software package. This also shows the positioning and shape of olivine (red) and ancillary phases (blue) present within the megacryst.

CHAPTER 5 – MINERAL CHEMISTRY

5.1. Clinopyroxene

BSE imagery, X-ray intensity maps and analytical data reflect the petrographic and compositional characteristics of the megacrysts. The data reveals that the host cpx (cpx) megacrysts are compositionally homogeneous with elemental compositions that are consistent with diopside (Figure 5.1). The major element chemical composition of cpx is quite narrow with major element compositions that are between $En_{42}Fs_{09}Wo_{48}$ and $En_{46}Fs_{08}Wo_{46.}$ The composition of the cpxs is presented in the Ca-Mg-Fe ternary plot with Wo-En-Fs end-member components expressed as percentages (Morimoto *et al.*, 1988). Major element analyses show that the cpx megacrysts have high Fe_2O_3 and TiO_2. The megacrysts also have low concentrations of Al_2O_3 (~5 and 7.5 wt.%), Na_2O (<0.5 wt.%) and Cr_2O_3 (<1 wt.%). Ca/(Ca+Mg) and Mg/(Mg+Fe^{2+}) ratios were calculated for the cpx megacrysts and have average values of 52.5 and 79.7 respectively. Na_2O content is very low (<1% Na_2O) and forms compact fields with Ca/(Ca+Mg).

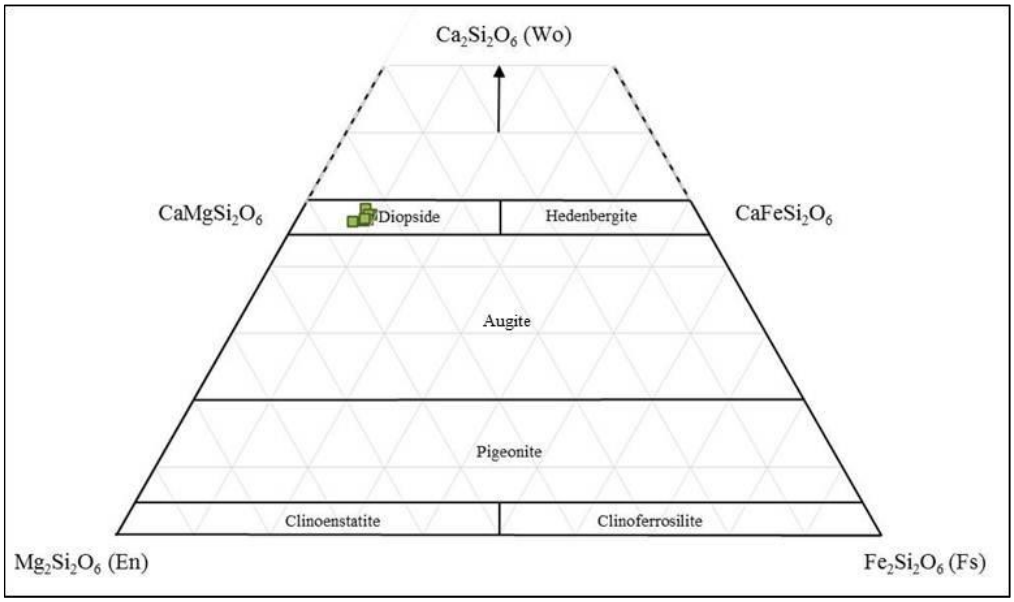

Figure 5. 1: A pyroxene ternary classification diagram showing the compositional characteristics of the Marion Island clinopyroxene megacrysts. The molar proportions of the megacrysts are expressed in terms of the Wo-En-Fs endmembers (Morimoto *et al.*, 1988).

A compilation of cpx from peridotitic and crustal sources taken from the precompiled collection of cpx data hosted on the GEOROC repository can be used as a benchmark in determining the nature of the Marion Island cpx megacrysts (GEOROC,2016). There are apparent differences in chemical data of the cpxs (Figure 5.2 and Figure 5.3).The Marion Island megacrysts have significantly higher content of FeO, TiO_2, Al_2O_3 and lower content of Na_2O and Cr_2O_3. In contrast, most peridotitic cpx are high in Cr_2O_3 (up to ~5 wt.%) and cluster in the low-Fe and low-Ti regions. The Marion Island megacrysts and other crustal megacryst display similar compositional trends and crustal signatures; however, the crustal cpx are more enriched in Al_2O_3 (up to ~12 wt.%), FeO (between 5 and 10 wt.%) and Na_2O (between 0.5 and 2.5 wt.%), and have low concentrations of CaO and TiO_2 and little to none Cr_2O_3 (<0.5 wt.%).

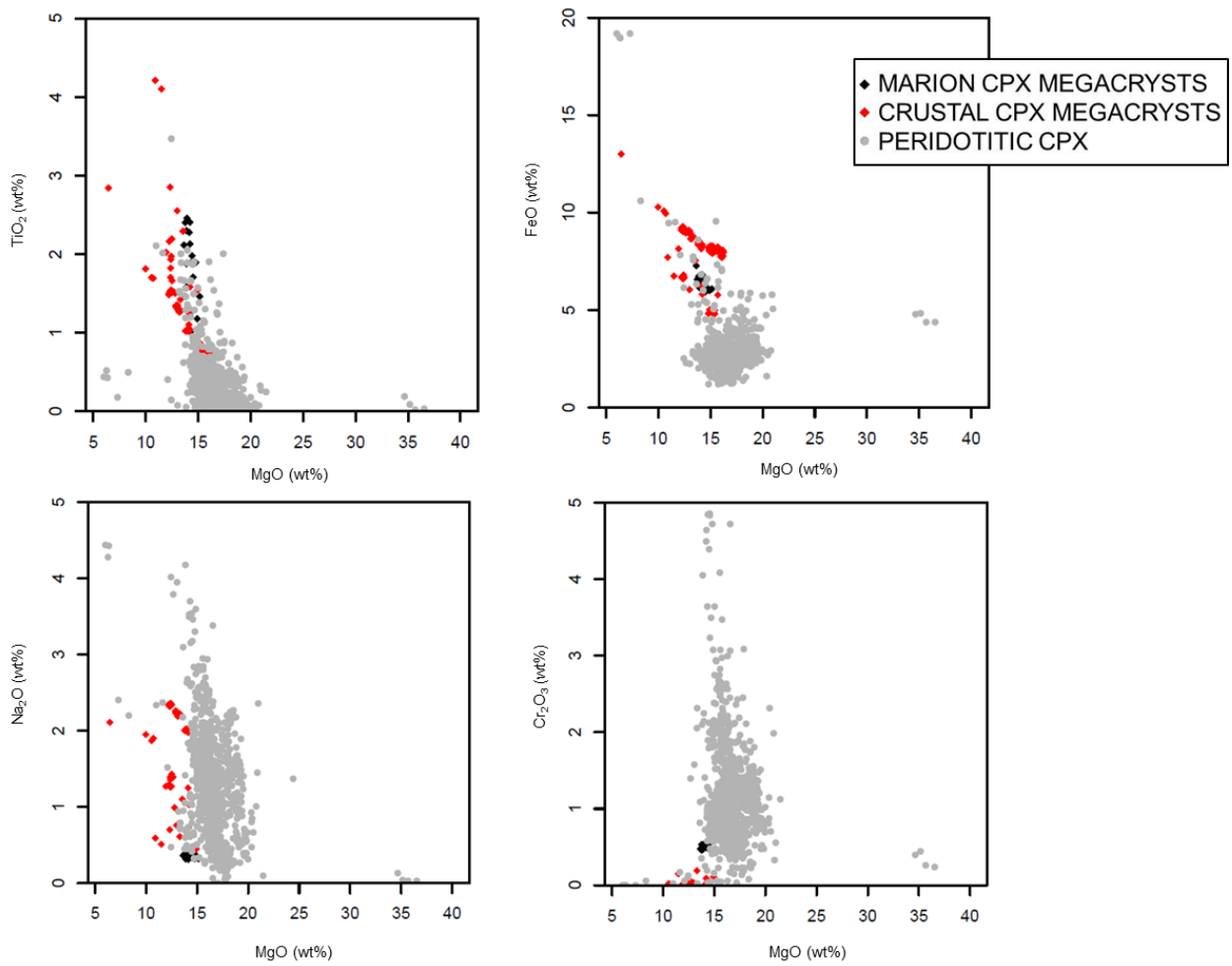

Figure 5. 2: Bivariate plots for clinopyroxene using MgO along the x-axis. Data of clinopyroxenes from a peridotite source and crustal megacrysts is given on the GEOROC database (GEOROC, 2016).

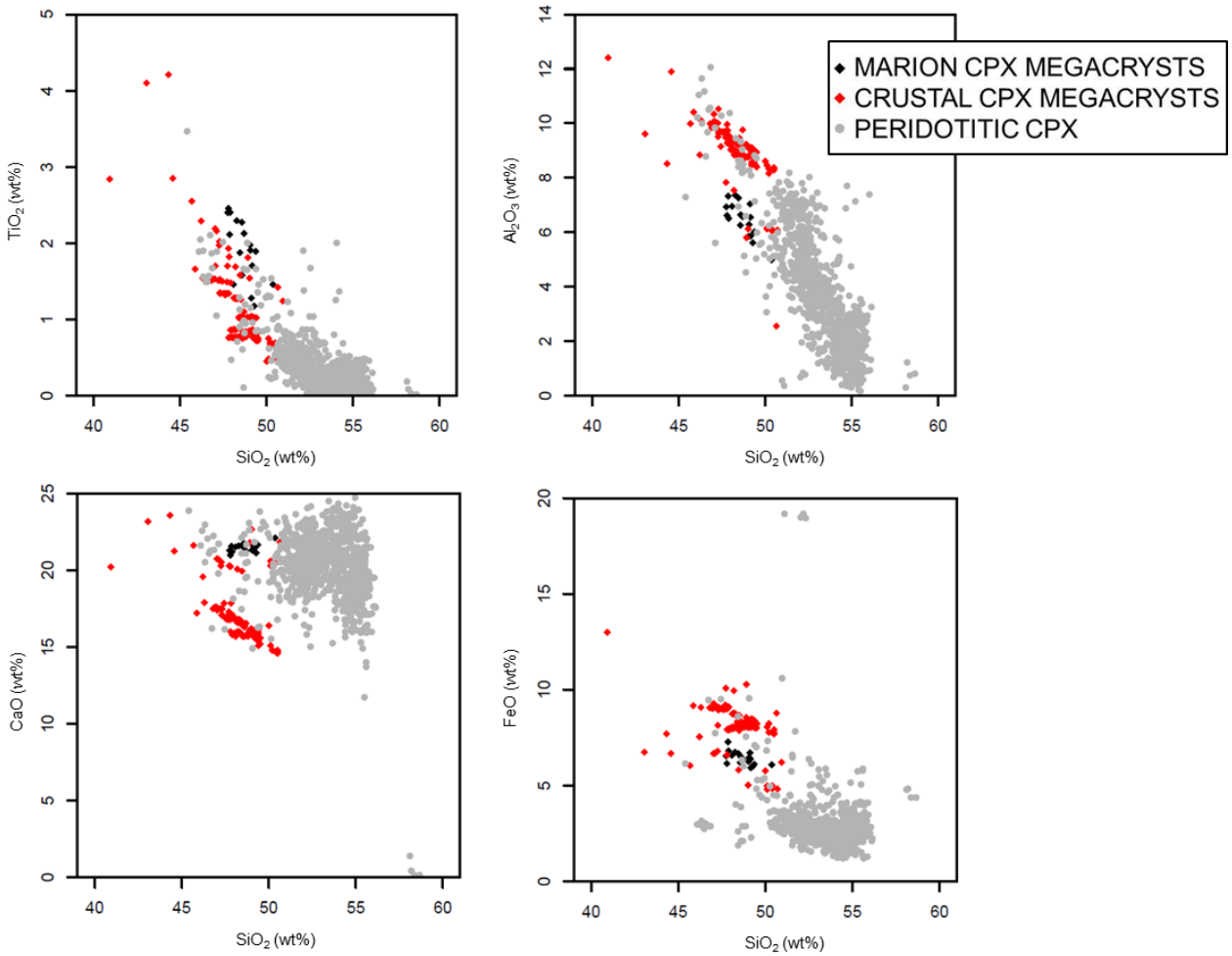

Figure 5. 3: Bivariate plots for clinopyroxene using SiO_2 along the x-axis. Data of clinopyroxenes from peridotites and megacrysts was taken from the GEOROC database (GEOROC, 2016).

Cr_2O_3 versus CaO and Na_2O versus Ca# binary plots have also been used to analyse the peridotitic nature of the cpx grains and demonstrates that peridotitic cpx are particularly Cr-rich and subcalcic as expected relative to the Marion and crustal cpxs (Figure 5.4).

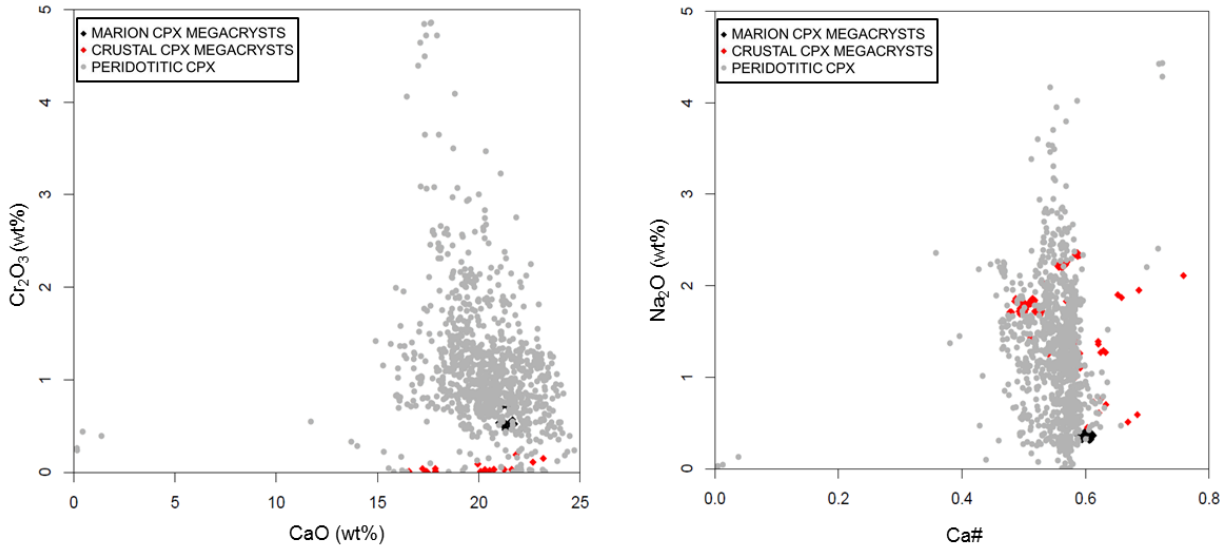

Figure 5. 4: Mineral chemistry binary plots of Cr_2O_3 versus CaO and Na_2O_3 versus Ca# for Marion Island clinopyroxene megacrysts and other clinopyroxenes with a crustal and peridotitic source. Data of clinopyroxenes from peridotites and megacrysts was taken from the GEOROC database (GEOROC, 2016).

Table 5. 1: Major element compositions of clinopyroxene megacrysts from Marion Island reported in wt.%.

Sample	2	2	2	4	4	4	4	4	4	4	4	4
Analysis	2_1	2_2	2_3	4_1	4_2	4_22	4_3	4_4	4_5	4_6	4_9	4_10
SiO_2	47.745	48.561	48.689	47.884	47.787	49.114	49.141	49.037	50.362	48.262	49.060	49.363
Al_2O_3	6.931	6.254	6.573	6.506	6.615	7.039	6.548	5.847	4.983	7.365	6.281	6.016
MgO	13.763	14.145	14.209	14.210	13.930	14.107	14.271	14.409	15.132	13.884	14.450	14.767
CaO	21.294	21.767	21.250	21.210	20.984	21.629	21.537	21.324	22.114	21.596	21.311	21.665
Fe_2O_3	0.991	0.751	0.827	1.568	0.379	1.674	1.824	0.713	1.448	1.303	0.893	1.081
FeO	5.552	5.450	5.553	5.241	5.771	5.032	4.565	5.539	4.634	5.434	5.557	5.026
MnO	0.156	0.121	0.128	0.092	0.123	0.119	0.144	0.147	0.112	0.103	0.099	0.140
Cr_2O_3	0.459	0.522	0.491	0.535	0.533	0.530	0.542	0.529	0.475	0.501	0.476	0.567
NiO	0.019	0.050	0.028	0.054	0.061	0.017	0.017	0.040	0.019	0.000	0.011	0.080
Na_2O	0.372	0.310	0.409	0.341	0.375	0.403	0.415	0.371	0.319	0.392	0.358	0.319
TiO_2	2.400	2.274	2.127	2.404	2.455	1.279	1.007	1.976	1.458	2.295	1.907	1.891
K_2O	0.021	0.031	0.019	0.031	0.054	0.029	0.007	0.006	0.013	0.026	0.039	0.041
Total	99.703	100.236	100.304	100.076	99.067	100.973	100.018	99.938	101.069	101.162	100.442	100.956

Sample	4	4	4	5	5	5
Analysis	4_11	4_12	4_13	5_1	5_2	5_3
SiO_2	47.856	48.452	48.575	49.160	48.078	49.272
Al_2O_3	7.327	7.256	6.637	5.863	6.951	5.613
MgO	13.631	13.882	13.880	14.516	13.749	14.901
CaO	21.568	21.600	21.498	21.424	21.520	21.132
Fe_2O_3	1.875	1.093	0.920	0.556	1.741	1.466
FeO	5.399	5.574	5.595	5.367	4.834	4.525
MnO	0.115	0.140	0.153	0.085	0.119	0.115
Cr_2O_3	0.475	0.469	0.487	0.704	0.531	0.705
NiO	0.044	0.000	0.028	0.000	0.015	0.040
Na_2O	0.362	0.321	0.317	0.332	0.381	0.366
TiO_2	2.113	1.875	1.580	1.704	1.458	1.175
K_2O	0.028	0.044	0.031	0.022	0.023	0.034
Total	100.793	100.705	99.701	99.733	99.400	99.344

5.2. Minerals present within the clinopyroxene megacrysts

The interior of the Marion cpx megacrysts appear to be highly fractured and porous with inclusions. The definite existence of minerals such as olivine, Fe-Ti-Al-Cr oxides, ilmenite sulphides and amphibole within the walls of the cpx megacrysts were confirmed with a microprobe and are described in this section.

5.2.1. Olivine

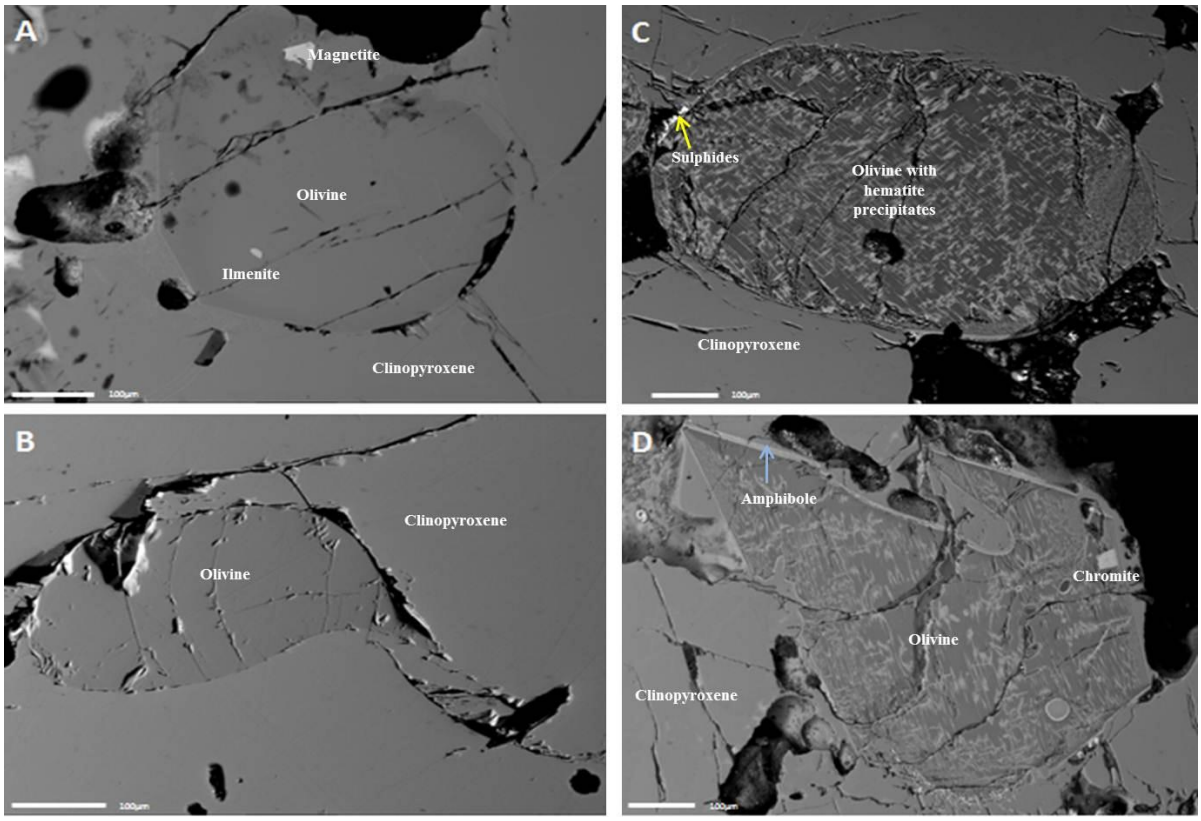

Figure 5. 5: Figures showing olivine inclusions within megacrysts of clinopyroxene (cpx). Images of the smooth and well-rounded olivine grains (A and B) with a euhedral crystal of magnetite included in olivine (A). (C) Oxidation of olivine producing hematite along the weak cleavage planes of olivine. (D) Secondary amphibole forming a flame-like rim between clinopyroxene and olivine (blue arrow). An intact chromite crystal is also seen within the olivine interior.

Minute sized crystals of olv constituting <5% of the total volume of the sample were identified along pore spaces of the megacrysts (Figure 5.5). These predominantly occur as aggregates of grains which are subrounded to well rounded, with conchoidal fractures producing curved surfaces. These vary in size from 200 to ~500µm. Both elemental maps and analytical data reveal that the olv inclusions are characterised by more Mg-rich compositions with an average composition of $Fo_{82.8}$-$Fa_{16.9}$-$Te_{0.2}$ (Table 5.2 through to Table 5.4). The olv

inclusions are essentially forsterite with molar proportions ranging between 79 and 83 wt.%. The olv inclusions also form compact fields and cover a broad range of iron mole fractions that are between 0.12 and 0.27. Mg# and NiO contents vary from 0.79 to 0.90 and 0.11 to 0.27 wt.% respectively. A variation in Ti content of between 0.069 and 0.810 wt.% is also noted.

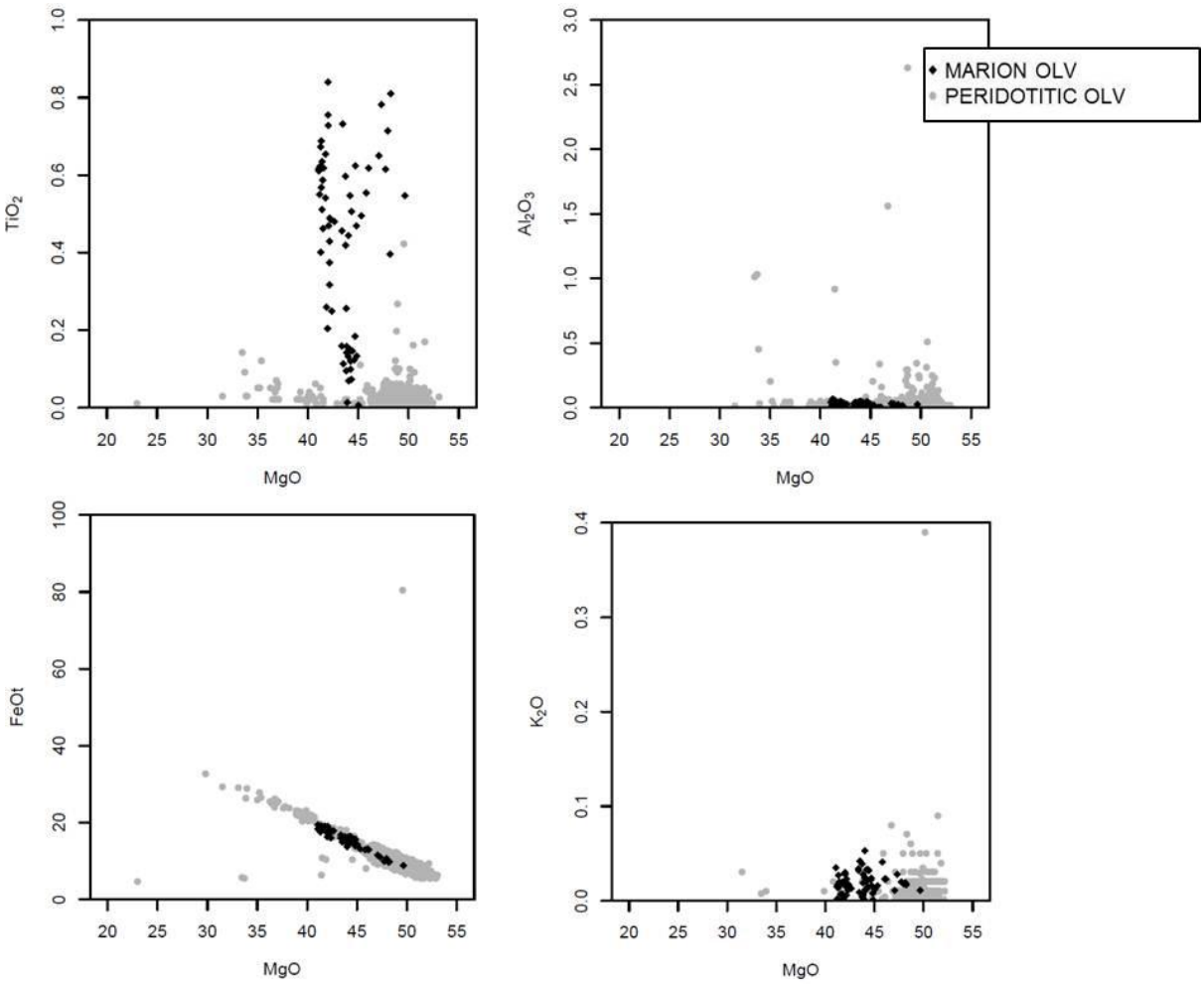

Figure 5. 6: Mineral chemistry binary plots for olv inclusions present within the cpx megacrysts and peridotites. MgO is used along the x-axis. Data used for the peridotitic olivine is taken from the GEOROC database (GEOROC, 2016).

Figures 5.6 and 5.7 show that there are apparent differences in chemical data for olv present within Marion cpx megacrysts and data for peridotitic olv taken from the GEOROC database (GEOROC,2016). Peridotitic olv are higher in NiO (<1.0 wt.%) and Cr_2O_3 (<0.4 wt.%). Differences are also apparent in TiO_2 versus MgO bivariate plots whereby TiO_2 of peridotitic olv falls within a restricted field of about 0-0.5 wt.%. TiO_2 content for the olv

inclusions stretches across the field up to ~0.9 wt.%. No significant chemical differences are observed for Al_2O_3 and K_2O.

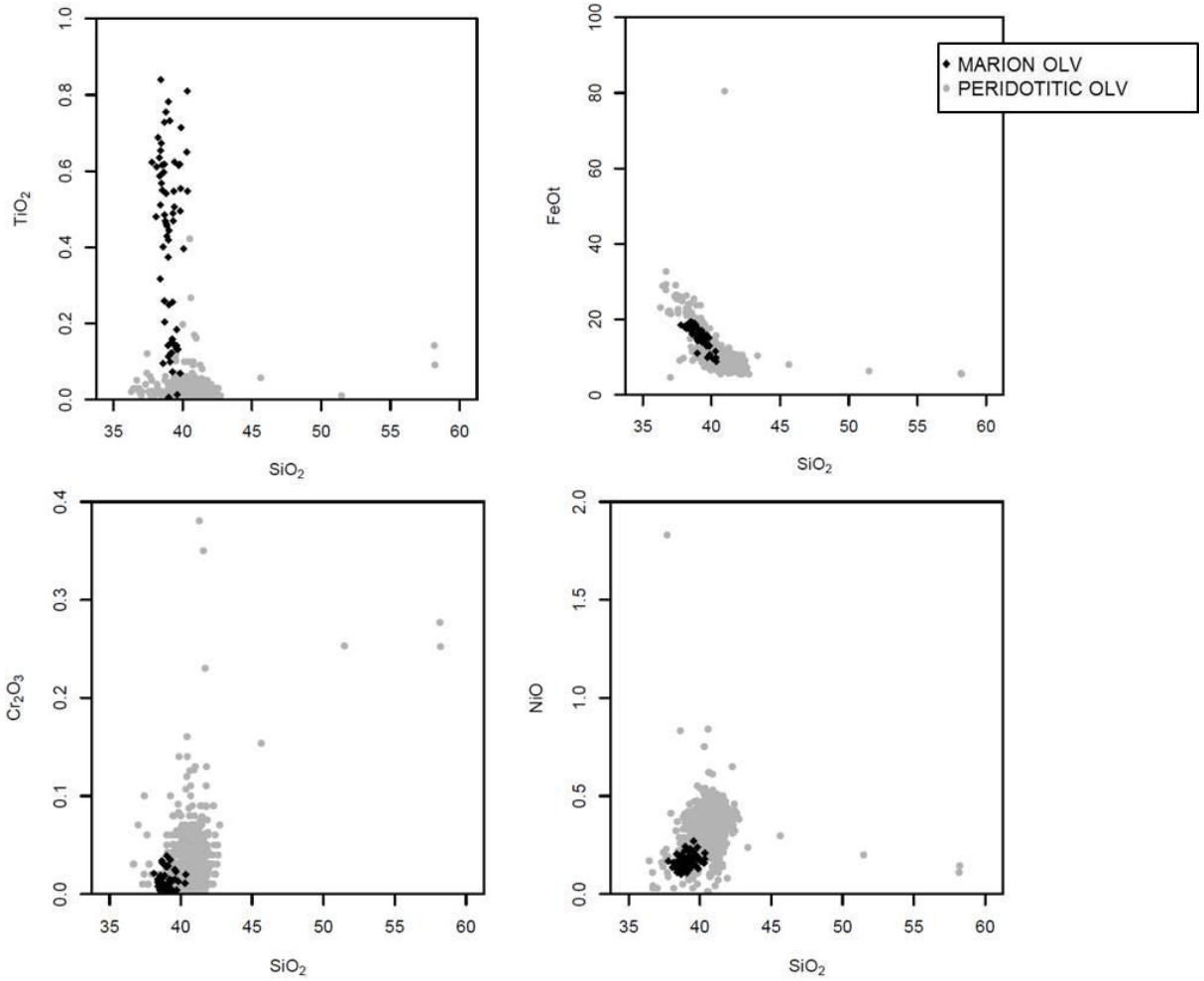

Figure 5. 7: Mineral chemistry binary plots for olv inclusions present within the cpx megacrysts and peridotites. SiO_2 is plotted along the x-axis. Data for the peridotitic olivine is provided on GEOROC database (GEOROC,2016).

Table 5. 2: Major element data for olivine inclusions present within the clinopyroxene megacrysts. All concentrations are reported as wt.%

Sample	2	2	2	2	2	2	2	2	2	2	2	2
Analysis	2_1	2_2	2_3	2_4	2_5	2_6	2_7	2_8	2_9	2_10	2_11	2_12
K_2O	0.007	0.000	0.017	0.029	0.015	0.014	0.002	0.000	0.020	0.035	0.000	0.002
CaO	0.226	0.222	0.227	0.260	0.247	0.241	0.220	0.228	0.278	0.217	0.220	0.252
SiO_2	38.397	38.583	38.450	38.700	38.528	38.463	37.779	38.112	38.318	38.515	38.804	38.678
Al_2O_3	0.038	0.055	0.039	0.043	0.017	0.036	0.066	0.045	0.034	0.040	0.051	0.030
MgO	41.754	41.276	41.263	41.952	41.159	41.330	41.211	41.083	41.413	41.074	41.504	41.846
FeO	19.076	18.749	18.942	17.602	18.135	18.066	18.512	18.359	18.780	19.386	18.606	18.070
MnO	0.229	0.227	0.271	0.222	0.267	0.204	0.237	0.249	0.220	0.247	0.209	0.263
Cr_2O_3	0.008	0.000	0.012	0.016	0.004	0.008	0.000	0.021	0.000	0.010	0.005	0.010
NiO	0.110	0.145	0.161	0.182	0.139	0.120	0.168	0.161	0.160	0.168	0.190	0.191
TiO_2	0.654	0.401	0.673	0.204	0.550	0.568	0.623	0.611	0.635	0.616	0.462	0.259
Total	100.499	99.670	100.055	99.210	99.061	99.050	98.818	98.869	99.858	100.308	100.051	99.601

Sample	2	2	2	2	2	2	2	2	2	2	2	2
Analysis	2_13	2_14	2_16	2_17	2_18	2_19	2_21	2_22	2_23	2_24	2_25	2_26
K_2O	0.017	0.028	0.016	0.011	0.023	0.013	0.007	0.017	0.024	0.005	0.039	0.032
CaO	0.205	0.223	0.212	0.230	0.240	0.217	0.231	0.181	0.283	0.280	0.249	0.304
SiO_2	38.389	38.676	38.417	38.689	38.374	38.071	38.681	38.342	39.005	39.266	38.968	38.863
Al_2O_3	0.059	0.031	0.047	0.015	0.042	0.026	0.031	0.007	0.049	0.022	0.021	0.014
MgO	41.402	42.021	41.998	42.282	42.152	42.637	41.554	41.475	44.025	43.816	43.746	43.386
FeO	19.128	16.287	17.365	17.827	17.780	17.829	18.611	18.296	15.989	16.236	16.175	15.966
MnO	0.242	0.216	0.227	0.213	0.214	0.238	0.286	0.242	0.251	0.231	0.279	0.233
Cr_2O_3	0.012	0.034	0.000	0.032	0.015	0.000	0.000	0.000	0.039	0.006	0.002	0.019
NiO	0.155	0.101	0.165	0.198	0.205	0.136	0.161	0.135	0.156	0.126	0.153	0.131
TiO_2	0.511	0.728	0.840	0.485	0.317	0.480	0.618	0.587	0.444	0.256	0.419	0.456
Total	100.120	98.345	99.287	99.990	99.362	99.647	100.180	99.282	100.265	100.244	100.051	99.404

Table 5. 3: (Continued) Major element data for olivine inclusions present within the clinopyroxene megacrysts. All concentrations are reported as wt.%

Sample	2	2	2	2	2	2	4	4	4	4	4	4
Analysis	2_27	2_28	2_29	2_30	2_31	2_32	4_1	4_2	4_3	4_4	4_15	4_19
K_2O	0.015	0.020	0.030	0.000	0.033	0.027	0.016	0.033	0.008	0.016	0.002	0.006
CaO	0.246	0.207	0.232	0.218	0.340	0.245	0.145	0.026	0.089	0.153	0.132	0.139
SiO_2	38.852	38.804	38.791	38.744	39.356	38.218	39.408	39.394	39.314	39.819	39.600	38.947
Al_2O_3	0.032	0.026	0.028	0.038	0.043	0.017	0.027	0.016	0.015	0.018	0.023	0.000
MgO	42.156	41.747	42.005	42.059	44.186	41.328	44.722	44.339	44.826	45.317	43.913	42.150
FeO	18.477	18.688	18.012	19.016	15.955	17.545	14.424	14.860	13.958	13.139	15.000	17.790
MnO	0.267	0.267	0.210	0.253	0.238	0.263	0.223	0.252	0.241	0.280	0.253	0.291
Cr_2O_3	0.000	0.010	0.000	0.000	0.004	0.000	0.000	0.014	0.013	0.000	0.015	0.003
NiO	0.148	0.143	0.131	0.156	0.138	0.158	0.184	0.172	0.140	0.239	0.152	0.174
TiO_2	0.429	0.541	0.755	0.469	0.547	0.688	0.624	0.506	0.469	0.495	0.013	0.374
Total	100.622	100.453	100.194	100.953	100.840	98.489	99.773	99.612	99.073	99.476	99.103	99.874

Sample	4	4	4	4	4	4	4	4	4	4	4	4
Analysis	4_21	4_22	4_23	4_25	4_26	4_27	4_28	4_29	4_30	4_31	4_32	4_33
K_2O	0.004	0.012	0.023	0.017	0.041	0.016	0.023	0.011	0.009	0.018	0.019	0.020
CaO	0.098	0.229	0.207	0.122	0.232	0.176	0.167	0.147	0.126	0.200	0.216	0.595
SiO_2	38.626	38.992	39.651	40.332	39.847	39.293	39.789	40.291	39.074	39.879	40.068	39.707
Al_2O_3	0.016	0.025	0.000	0.000	0.003	0.021	0.002	0.032	0.020	0.010	0.015	0.024
MgO	43.734	45.026	46.167	48.239	45.803	42.170	46.036	47.059	43.456	47.947	48.173	47.720
FeO	16.283	14.326	12.947	9.841	12.946	17.060	13.130	11.535	15.824	10.662	9.725	9.909
MnO	0.239	0.211	0.301	0.228	0.218	0.311	0.220	0.266	0.263	0.259	0.252	0.275
Cr_2O_3	0.000	0.000	0.000	0.000	0.000	0.004	0.000	0.011	0.028	0.000	0.000	0.004
NiO	0.165	0.167	0.189	0.179	0.189	0.183	0.182	0.158	0.108	0.129	0.166	0.143
TiO_2	0.597	0.006	0.000	0.810	0.554	0.489	0.618	0.650	0.732	0.714	0.396	0.615
Total	99.762	98.994	99.485	99.768	99.837	99.723	100.176	100.160	99.640	99.818	99.030	99.012

Table 5. 4: (Continued) Major element data for olivine inclusions present within the clinopyroxene megacrysts. All concentrations are reported as wt.%

Sample	4	4	6	6	6	6	6	6	6	6	6	6
Analysis	4_34	4_35	6_1	6_2	6_3	6_4	6_5	6_6	6_8	6_11	6_12	6_13
K_2O	0.028	0.011	0.015	0.012	0.013	0.025	0.053	0.010	0.019	0.000	0.022	0.032
CaO	0.340	0.230	0.181	0.183	0.170	0.204	0.213	0.234	0.204	0.207	0.153	0.170
SiO_2	38.965	40.345	39.255	39.815	39.109	39.566	39.346	39.660	38.579	39.090	39.189	39.323
Al_2O_3	0.029	0.025	0.029	0.022	0.022	0.024	0.021	0.015	0.041	0.005	0.044	0.035
MgO	47.312	49.649	44.329	44.056	44.240	44.009	44.014	43.998	43.821	44.246	44.613	44.420
FeO	11.046	8.828	16.451	15.075	15.709	13.724	15.435	15.845	16.144	15.591	15.610	15.671
MnO	0.225	0.266	0.182	0.176	0.221	0.251	0.209	0.187	0.193	0.175	0.217	0.241
Cr_2O_3	0.028	0.020	0.035	0.013	0.000	0.025	0.001	0.023	0.019	0.029	0.013	0.000
NiO	0.182	0.209	0.227	0.179	0.178	0.193	0.228	0.201	0.192	0.185	0.216	0.230
TiO_2	0.782	0.547	0.073	0.069	0.120	0.142	0.145	0.132	0.095	0.099	0.123	0.146
Total	98.937	100.130	100.777	99.600	99.782	98.163	99.665	100.305	99.307	99.627	100.200	100.268

Sample	6	6	6	6	6	6	6	6
Analysis	6_14	6_15	6_16	6_17	6_18	6_19	6_20	6_21
K_2O	0.007	0.020	0.028	0.001	0.042	0.024	0.017	0.034
CaO	0.152	0.196	0.199	0.165	0.196	0.178	0.218	0.192
SiO_2	38.935	39.210	39.267	39.550	38.965	39.565	39.005	39.242
Al_2O_3	0.046	0.012	0.010	0.023	0.040	0.045	0.034	0.034
MgO	43.851	44.131	43.852	44.850	43.519	44.685	42.376	43.370
FeO	14.975	16.248	15.083	15.642	14.953	15.705	16.026	16.729
MnO	0.232	0.210	0.191	0.184	0.166	0.188	0.227	0.244
Cr_2O_3	0.005	0.015	0.001	0.001	0.009	0.000	0.006	0.011
NiO	0.222	0.164	0.191	0.270	0.243	0.215	0.155	0.185
TiO_2	0.142	0.151	0.158	0.133	0.113	0.184	0.249	0.159
Total	98.567	100.357	98.980	100.819	98.252	100.789	98.313	100.200

5.2.2. Fe-Ti-Cr-Al Oxides

Oxides occur in the form of fragmented crystals or euhedral crystals with intact crystal faces confined to olv grains. Spinel group minerals, hematite and ilmenite are clearly seen in both BSE images and elemental maps of the cpx megacrysts. Compositional variations between the identified oxide minerals are quite significant with all major element data reported in Table 5.5. All the identified phases are further described in the following sub-sections.

5.2.2.1. Spinel group minerals

Magnetite, ferrian pleonaste and chromite were observed as spinel phases in the studied cpx megacrysts and occur as euhedral or fragmented crystals within olv. Magnetite also developed as tiny blebs which may cluster to form a fine strip around the olv inclusions. These spinel group minerals have a wide range of compositions for Al_2O_3 (0.1 – 27 wt.%), MgO (0.3 – 13 wt.%) and TiO_2 (1 – 9wt.%). The spinel phases are further characterised by very high Cr_2O_3 concentrations and very low contents of NiO (<0.3 wt.%) and MnO (<0.4 wt.%). Cr# (Cr# = Cr/(Cr + Al)) was calculated for magnetite and ferrian pleonaste and ranges from 1 - 14 and 24 - 50 respectively (Figure 5.8).

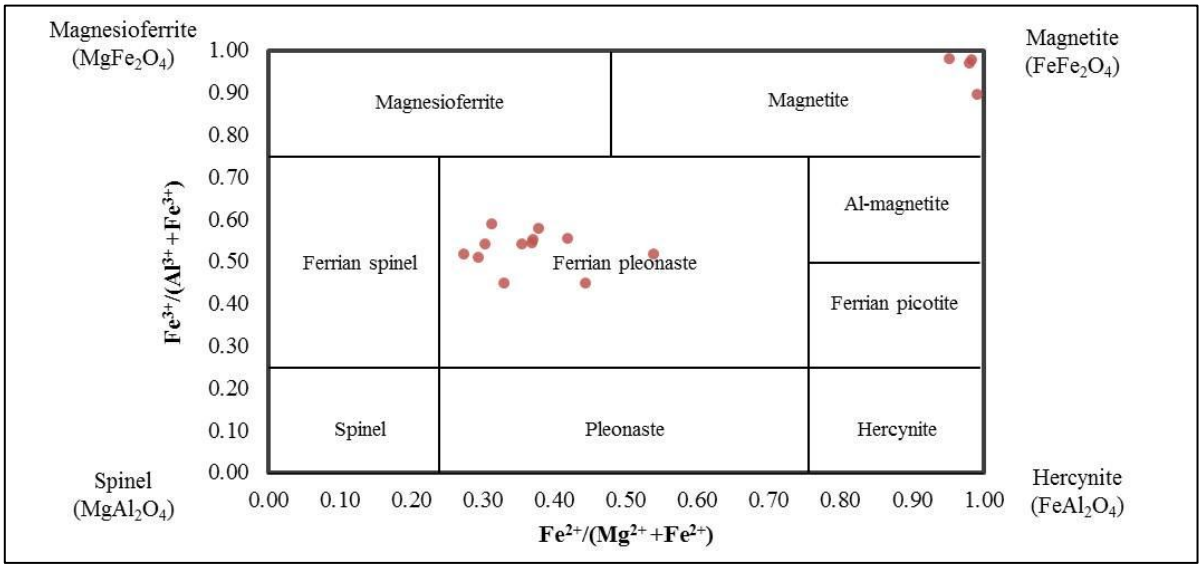

Figure 5. 8: A chemical classification diagram for spinel group minerals according to Gargiulo *et al.* (2013) classification. This classification is dependent on the exchange of the trivalent cations in the 'X' structural site.

5.2.2.2. Ilmenite

Ilmenite is found exclusively in a number of olv inclusions present within the Marion cpx megacrysts (Figure 5.5D). It occurs as single, euhedral crystals which may in other instances, occur as relict fragments. The ilmenite inclusions have a narrow compositional range with extremely low MgO values ranging from ~0.03 to 0.02 wt.% (Mg#= 0.06), Al_2O_3 (0.09 – 0.11 wt.%), and moderate to high average FeO and TiO_2 content of about 37.5 wt.% and 56.2 wt.% respectively. The electron microprobe results are reported in Table 5.3.

5.2.2.3. Hematite

Hematite precipitates orientated along weak cleavage planes in some of the olv inclusions (Figure 5.5C and Figure 5.5D). It typically forms irregular lamellae along poor cleavage planes on {010} and {110}, cross-cutting at an angle between 46 and 98°. Reliable Raman spectrum is given below as the lamellae are often too small for electron microprobe analysis (Figure 5.10).

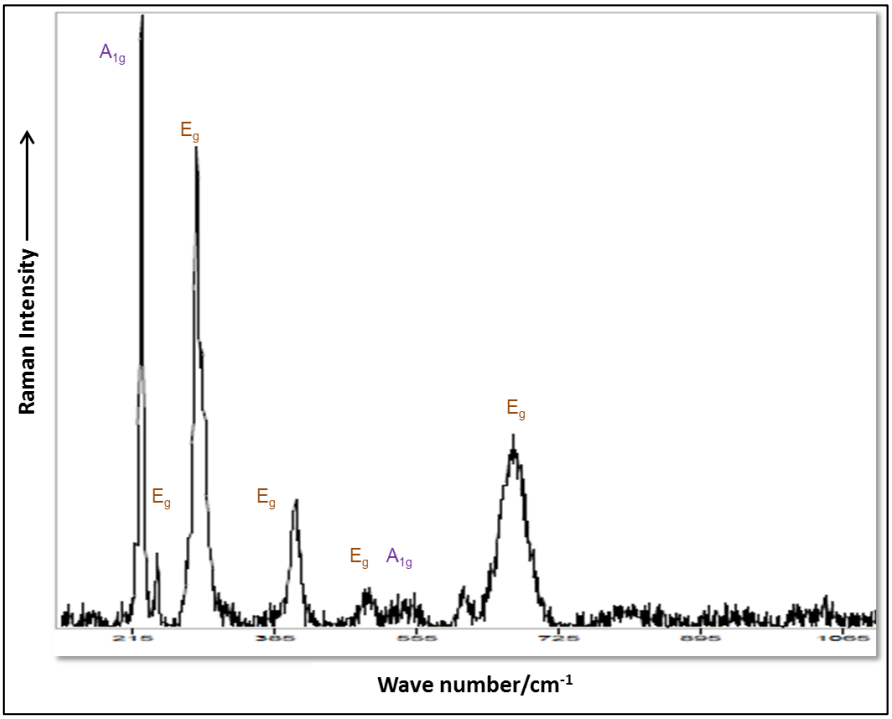

Figure 5. 9: A clear spectrum of hematite occurring along weak cleavage planes in olivine. A clear and distinct 2A1g 5Eg hematite vibrational mode is observed.

Table 5. 5: Selected major element data for Fe-Ti-Cr-Al oxides occurring within the clinopyroxene megacrysts. All data is reported as wt.%.

Sample	2	2	2	2	2	2	4	4	5	5	5	5	5
Analysis	2_1	2_2	2_3	2_4	2_5	2_6	4_4	4_5	5_1	5_2	5_3	5_5	5_12
SiO_2	0.040	0.086	0.128	0.112	0.123	0.087	0.101	0.377	0.046	0.063	0.127	0.604	0.091
TiO_2	4.010	8.625	6.546	8.963	8.467	2.769	2.925	3.674	3.414	2.488	4.538	4.044	6.442
Al_2O_3	23.480	22.234	21.693	22.168	22.107	21.427	21.666	27.048	25.644	29.443	14.838	21.836	16.739
Cr_2O_3	11.560	12.486	12.327	12.717	12.631	31.434	29.410	16.817	14.183	13.934	22.340	24.568	21.951
V_2O_3	0.793	0.554	0.538	0.531	0.538	0.115	0.132	0.141	0.268	0.175	0.199	0.209	0.398
Fe_2O_3	29.240	20.221	24.367	18.971	20.244	12.579	14.109	18.315	24.277	20.912	27.074	16.694	20.162
FeO	19.135	25.368	24.502	25.202	25.569	21.048	20.744	23.131	24.159	24.362	21.498	19.315	24.969
MnO	0.264	0.178	0.379	0.290	0.164	0.219	0.342	0.217	0.331	0.206	0.361	0.387	0.170
MgO	13.155	11.839	10.955	11.958	11.614	10.990	11.215	10.925	9.863	9.470	11.160	13.251	10.152
NiO	0.140	0.187	0.201	0.186	0.190	0.142	0.127	0.148	0.184	0.222	0.160	0.166	0.138
Total	101.816	101.778	101.636	101.098	101.646	100.810	100.771	100.793	102.368	101.274	102.296	101.074	101.212

Sample	5	5	5	5	4	4
Analysis	5_6	5_7	5_9	5_10	4_7	4_8
SiO_2	0.210	1.762	0.303	0.268	0.097	0.114
TiO_2	1.348	0.273	1.032	2.738	56.006	56.333
Al_2O_3	0.723	0.381	0.807	1.925	0.090	0.113
Cr_2O_3	0.033	0.016	0.014	0.115	0.000	0.000
V_2O_3	0.008	0.000	0.061	0.114	1.465	1.403
Fe_2O_3	66.222	65.606	66.266	61.357	0.000	0.000
FeO	32.488	30.799	31.875	33.980	37.516	37.418
MnO	0.019	0.115	0.140	0.000	1.630	1.963
MgO	0.417	2.010	0.552	0.369	0.035	0.021
NiO	0.009	0.000	0.012	0.000	0.000	0.003
Total	101.477	100.962	101.062	100.866	96.839	97.368

5.2.3. Sulphides

Microscopic aggregates of sulphides are also identified within the cpx megacrysts. These cluster along the cpx-olv boundary also occurring as small isolated grains within cpx. Sulphides constitute <5% of the sample and have compositions which are compatible to pyrrhotite. Fe varies widely for the sulphide grains from 51 to 59 wt.%. Zn content is very low ranging between 0 and 0.06 wt.%. Ni/(Ni+Fe) ratios are distributed within a range of 9 and 14. However, microprobe data shows that the sulphide mineral grains are slightly more Ni-rich (between 6.2 and 8.6 wt.%) than a typical pyrrhotite (Ni <1wt.%). This high Ni content suggests that the pyrrhotite aggregates denote Ni-poor monosulphides. Some limitations encountered when deriving geochemical data include the removal of some of the grains due to repolishing of the sample surface. Consequently, a limited number of analyses are reported in Table 5.6.

Table 5. 6: Elemental analyses for the selected sulphide minerals is reported as wt.% and normalised to 100%.

Sample	2	2	2	2	2	2
Analysis	2_3	2_4	2_5	2_6	2_7	2_8
S	38.964	39.246	34.582	39.755	39.693	38.964
Fe	53.564	54.177	59.074	53.658	51.593	53.564
Zn	0.031	0.000	0.055	0.014	0.101	0.031
Ni	7.441	6.578	6.289	6.574	8.613	7.441
Total	100.000	100.000	100.000	100.000	100.000	100.000

5.3. Amphibole

The amphibole found along the cpx-olv boundary is secondary in nature. These have been recognised by means of microprobe analyses as Mg- and Fe-rich hornblende according to Leake *et al*. (1997) classification. No discrete grains were identified but rather occur as a secondary product likely due to replacement of cpx by hornblende during cooling in a somewhat hydrous environment, or a probable reaction took place between cpx and the mafic alkaline melt that transported the megacrysts to the surface. Due to difficulties in telling cpx apart from amphibole on BSE images, limited compositional data was collected and is presented in Table 5.5. However, elemental maps and transects taken using a microprobe show a distinct variation in composition along the cpx-olv boundary. This mineral phase is

strongly enriched in K, Al, Na and Ti, and depleted in Mg and Ca when compared to cpx and olv (Figure 5.11).

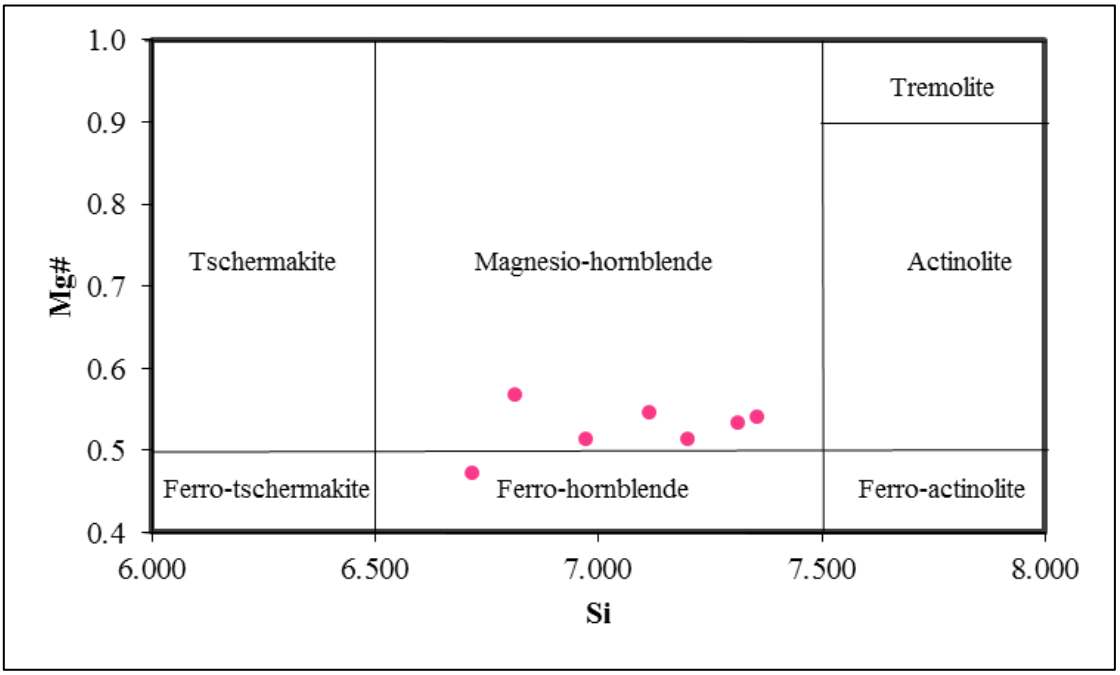

Figure 5. 10: Amphibole classification diagram showing all amphibole microprobe data. These are plotted in accordance with the Leake *et al*. (1997) classification.

Table 5. 7: Major element data for amphibole occurring within the studied samples. Element concentrations are presented as wt.%.

Sample	2	2	2	2	4	4	4
Analysis	2_1	2_8	2_9	2_16	4_21	4_22	4_23
SiO_2	46.349	53.185	53.330	47.809	51.378	50.651	49.270
TiO_2	3.997	3.145	2.671	3.492	3.860	3.783	4.422
Al_2O_3	15.121	17.163	16.926	15.164	16.215	16.229	16.076
Cr_2O_3	0.006	0.014	0.028	0.016	0.033	0.031	0.019
FeO	13.007	8.190	8.291	9.658	9.185	8.879	9.126
MnO	0.248	0.163	0.119	0.166	0.160	0.163	0.152
NiO	0.018	0.000	0.000	0.014	0.000	0.000	0.000
MgO	6.511	5.251	5.467	7.095	5.439	5.975	5.408
CaO	8.642	7.519	7.662	13.649	6.283	7.458	9.427
Na_2O	1.859	2.744	2.513	0.073	3.508	3.121	1.974
K_2O	2.146	0.401	0.414	0.237	1.251	0.848	1.581
Total	97.903	97.773	97.420	97.373	97.312	97.140	97.456

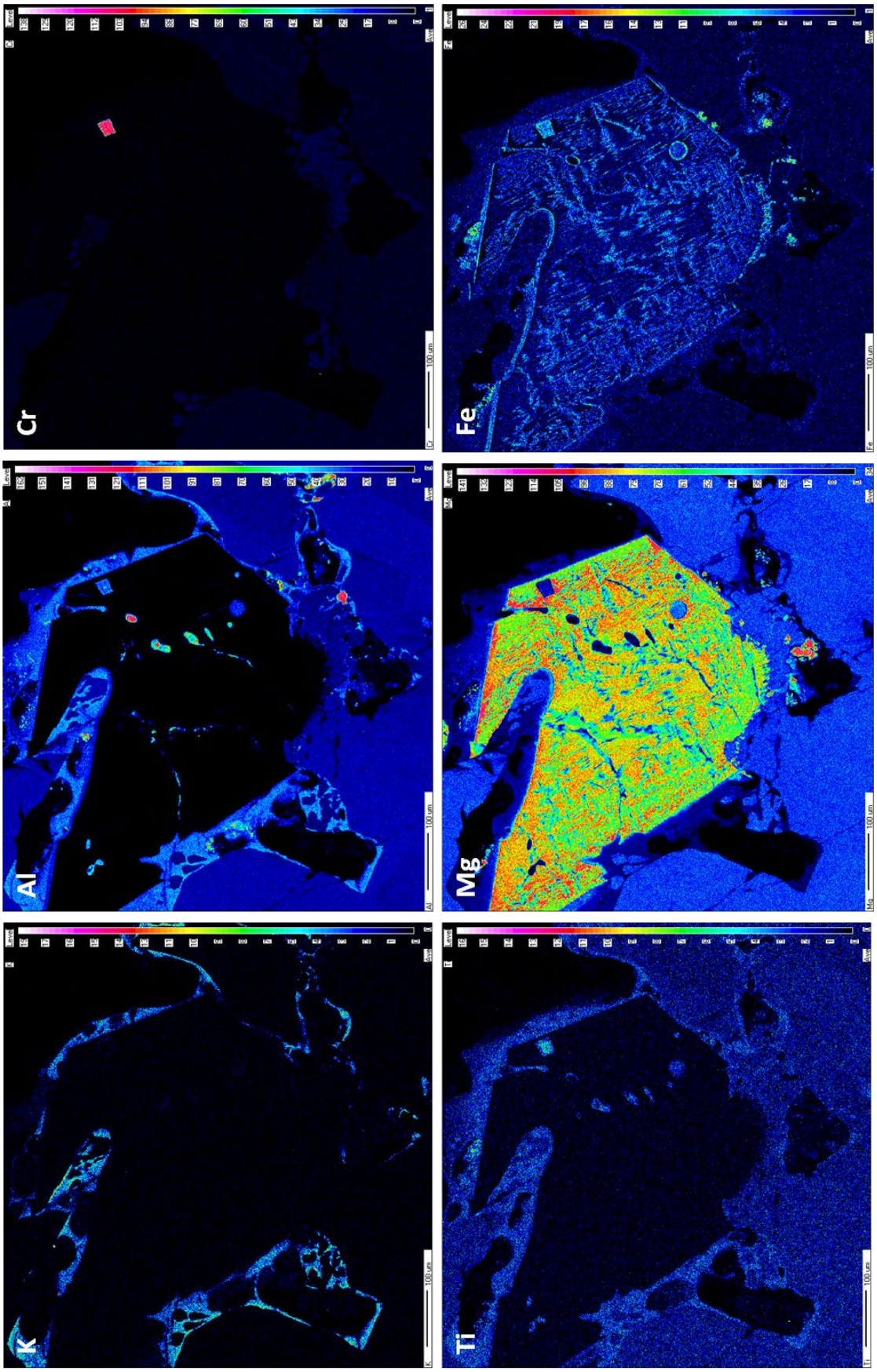

Figure 5. 11: Elemental maps taken using an EPMA showing elemental abundances of minerals present within the host clinopyroxene megacryst. Clinopyroxene and amphibole are more enriched in Ca while olivine is recorded as having the highest Mg concentrations. Secondary amphibole forms a rim along the cpx-olv boundary. This mineral phase is more enriched in K, Al, Ti with respect to other identified phases. A chromite inclusion having high contents of Fe and Cr is also noted within the olivine interior.

CHAPTER 6 – DISCUSSION

Numerous suggestions have been made in determining the origin and formation mechanisms involved in developing such large cpx crystals. This is also relevant in determining the origin of the mineral phases present within the megacrysts. This makes comparing the peculiarities and differences in compositions of the Marion Island megacrysts, crustal megacrysts and peridotites worth evaluating. The influence of geological constraints on the formation of the clinopyroxene megacrysts will also be discussed in this chapter.

6.1. The nature of the megacrysts based on its mineralogical constraints, formation mechanism and origin

A cpx ternary diagram showing the composition of Marion Island cpx megacrysts depicts that the crystals are mainly diopside. The megacrysts have retained their non-typical euhedral shape and were previously interpreted as having a characteristic zoning pattern known as patchy zoning (Botha, 2013). Botha (2013) further suggests that patchy zoning occurs in different varieties and forms gradual or step-like boundaries within cpx, which is present in the form of diopsidic and augitic cpx. This type of zoning often indicates that diffusion processes were active as magma sought to re-equilibrate with the crystals along its pore spaces (Streck, 2008). This has led to the conclusion that the dominant process responsible for the formation of this uncommon zoning pattern is diffusion (Brugger and Hammer, 2010).The integration and re-evaluation of iron microprobe Al-, Si-, Ti-, Cr-,Mg-K-alpha chemical distribution maps (Botha, 2013), tomography images and geochemical data strongly suggests that the mineral previously identified as augite is actually an amphibole. This finding corresponds very well with the dark patches observed in the tomography slices. The major element compositional data for amphibole is reported in Table 5.4. Amphibole occurs as a secondary product likely formed by replacement during cooling. Another possible explanation for the formation of amphibole can be related to a mafic alkaline melt reacting with the megacrysts along its pores and fractures during transport to the surface.

The host cpx megacrysts have a narrow compositional margin that is between $En_{42}Fs_{09}Wo_{48}$ and $En_{46}Fs_{08}Wo_{46}$. The cpx megacrysts are more Fe-rich and Ti-rich with

Cr_2O_3 concentrations ranging from 0.069 wt % to 0.81 wt %. The megacrysts also have a narrow Mg#, 79 – 82. Mantle cpx are typically less enriched in FeO when compared to crustal-derived cpx. These are also distinguishable from crustal cpx by the high Cr_2O_3 concentrations with minimum and maximum values that are between 0.3 w.% and 0.9 wt.% (Selyatitsikii and Reverdatto, 2011).

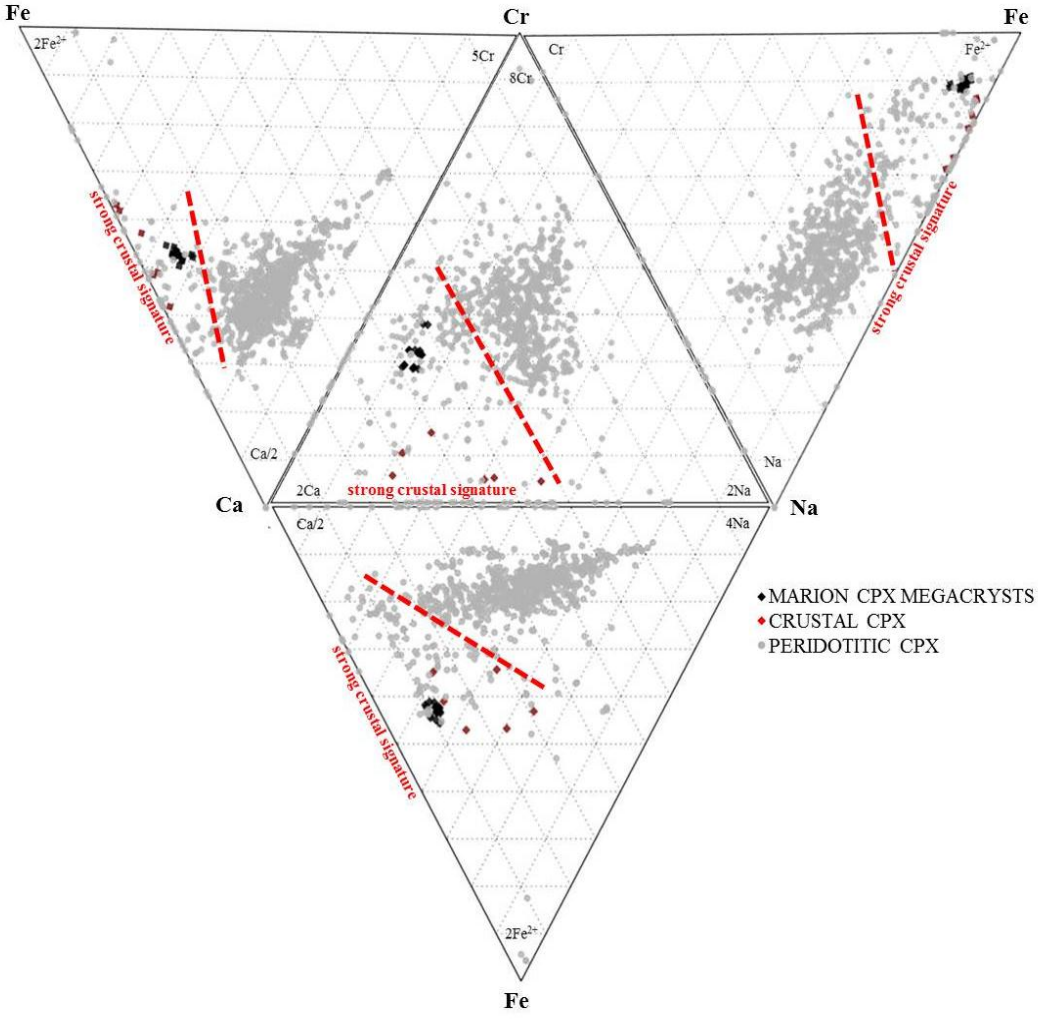

Figure 6. 1: Na-Ca-Cr-Fe ternary diagram showing distinct compositional differences between the Marion Islaned clinopyroxenes megacryst, crustal megacrysts and mantle cpx in peridotites (Quirt, 2004). This shows two distinct groupings which can be separated by an empirical field separator line created from a compilation of data from Fipke *et al.* (1989).

The main differences in composition of cpx megacrysts from Marion Island, other crustal megacrysts and cpx from mantle peridotites are further summarised in Figure 6.1. The Na-Ca-Cr-Fe diagram clearly shows that the Marion Island cpx megacrysts predominantly have a crustal signature. We can further delineate that the cpx megacrysts have a mid-crustal

signature a as these can be discriminated from other crustal cpx megacrysts having much higher Fe concentrations and very little Cr.

Olv is one of the most common minerals to crystallise in mantle-derived peridotites. These are directly sourced from the mantle and thus provide valuable information useful in unravelling the chemistry of the mantle. Olv inclusions are frequently ripped off the walls of the magmatic channels and conveyed to the surface by violent magmas. Carter (1970) published a research paper in which the textural and chemical nature of xenoliths from New Mexico is studied. The texture and chemistry of the xenoliths and xenocrysts were further cited as decisive factors in establishing a classification scheme for xenoliths. In the paper, the author states that a source olv inherited from a mantle would have a forsterite signature of ≥ 88wt.%. Olv crystals which have rather crystallised from the melt will most likely have a lower forsterite content which is less than 86wt.%. High Fe- mole fractions that are between 0.14 and 0.44 were also calculated for crustal olv. Fe-mole ratios of olv from mantle peridotites typically lie between 0.04 and 0.11 and often have NiO concentrations >0.3 wt.% (Selyatitsikii and Reverdatto, 2011).

The Fe-mole ratio of the olv inclusions present within the cpx megacrysts range between 0.10 and 0.21. These are also characterised by very low concentrations of Cr_2O_3 (0 to 0.04). The analysed olvs also have low NiO concentrations that are between 0.11 and 0.27 wt.% and a forsterite content that is from 79 wt.% to 89 wt.%. These findings strongly suggest that olvs are sourced at different depths with some originating from the mantle and others derived at depths that are closer to the crust.

It is quite evident from olv data and Figure 6.2 that Mg# for olv with hematite precipitates is higher compared to those without it. This provides important clues to the origin of the olv inclusions as well as providing useful information regarding processes that led to the formation of hematite.

The oxidation of mantle olv often produces hematite precipitates within the interior of olv. The occurrence of hematite precipitates has further been reported in lab experiments and in nature with olv being oxidised at high temperatures (Champness, 1970; Kohlstedt and

Vander Sande, 1975). With the removal of Fe, its compositions become more Mg-rich. The recurring appearance of hematite lamellae within the olv crystals present within the Marion Island cpx megacryst suggests that oxidation is an essential mechanism that led to its formation (Hwang *et al.*, 2008). Hematite is typically associated with an oriented silicate phase within olv and can be represented by the formula below:

$$2Fe_2SiO_4 \text{ (olivine)} + O_2 = 2Fe_2O_3 \text{ (hematite)} + 2SiO_2.$$

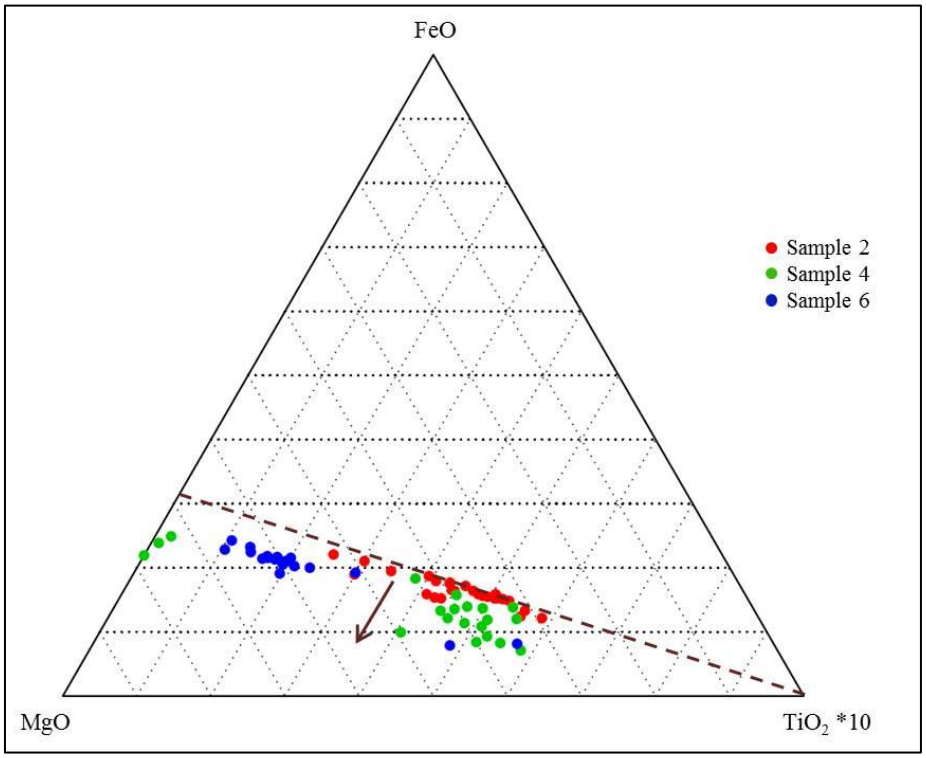

Figure 6. 2: MgO-FeO-TiO_2[10] ternary diagram showing the composition of olivine changing from ones with a constant initial Mg:Fe ratio to some becoming enriched in Mg. TiO_2 concentrations also vary significantly for the olivine inclusions suggesting that the olivines are metamorphosed.

However, a silicate phase was not observed as an oxidation product in the present study. The lack of a silicate phase in association with hematite and the presence of hematite within olv in the studied samples presented difficulties in the application of numerous oxidation scenarios (Khisina and Wirth, 2002; Dyar *et al.*, 1998 and Ingrin and Skogby, 2000). The only convincing alternative relative to the formation of hematite precipitates in olv requires that the exhumation history of olv be taken into account (Hwang *et al.*, 2008). Exhumation in this case, could be driven by magma ascent. Olv is transported by magma from mantle depths to shallower depths in the earth's crust where temperatures are between

550 °C and 650 °C. However, this process requires H to be incorporated within olv. H can be incorporated in the crystal lattice of an anhydrous olv during magma ascent to shallower depths. H diffusion and the oxidation of Fe^{2+} to Fe^{3+} will thus result in the precipitation of hematite along the weak cleavage planes or dislocations of olv (Hwang *et al.*, 2008). This process is referred to as dehydrogenation- oxidation (Ingrin and Skogby, 2000). It forms the Fe^{3+} required for hematite to precipitate through the following reactions:

$$2Fe^{2+} + OH^{-} = 2Fe^{3+} + 2O^{2-} + H_2 \quad (1)$$

$$2Fe^{2+} + 2H^{+} = 2Fe^{3+} + H_2 \quad (2)$$

Fe^{3+} would be released from the olv crystal lattice resulting in hematite precipitating within olv at shallower depths through the following reaction:

$$x(FeMg)_2SiO_4 + 3O = Fe_2O_3 + yMg_2SiO_4.$$

Dehydrogenation is often accompanied by the generation of secondary metamorphic olv (De Hoog *et al.*, 2014). Secondary metamorphic olv is often marked by very high TiO_2 content of up to 0.85 wt.%, correlating with H_2O of up to 0.7 wt.% being introduced into the system. The heavy fracturing of studied olv inclusions together with the occurrence of magnetite further supports the secondary nature of the olv inclusions. Variation in TiO_2 content of the olv inclusions is also worth mentioning (Figure 5.6 and Figure 6.2). Both images show a sparse distribution of TiO_2 concentrations for olv. TiO_2 ranges between 0 wt.% and 0.81 wt.%. The olv grains can thus be subdivided into several generations based on TiO_2 content. De Hoog *et al.*, (2014) reported that early metamorphic olv is Ti-poor (0-0.025 wt.%) and second generation metamorphic olv is Ti-rich with TiO_2 content of up to 0.85 wt.% .the olv inclusions found in sample 2 mostly fall can be classified as early metamorphic olv whilst the olv included in sample 4 and sample 6 fall within second generation olv group.

Magnetite, chromite, spinel and ilmenite occur as discrete euhedral and fragmented crystals within olv. These are homogeneous in composition and tend to be less susceptible to oxidation. The euhedral nature of these mineral phases and also their presence within forsteritic olv suggests that these are primary phases. Magnetite appears as both euhedral crystals and also as blebs along the olv grain boundary. The latter points to magnetite crystallising after a volcanic eruption and the lava cools on the surface.

6.2. Geological constraints on the conditions of formation of the clinopyroxenes megacrysts

In order to crystallise these giant crystals of clinopyroxene, a volatile-rich basaltic magma is required as means of triggering a large degassing event. The introduction of water to the system often has a great impact on seafloor magmatic processes (Feig *et al.*, 2006). These processes range from partial melting to fractionation (Asimow and Langmuir, 2003). Water makes up a considerable fraction of the mantle, but just how much is present and how it is distributed within the mantle still remains a subject of debate. The mantle could be holding up to 0.2 % water with hydrous minerals and nominally anhydrous minerals such as olivine and pyroxene serving as storage sites in the form of structural defects within the crystals (Bhattacharya, 2012). However, water capacity of minerals often relies on temperature, pressure and mineral composition. Water often has a negative effect on the chemical bonds of minerals and thus disturbing their phase stability.

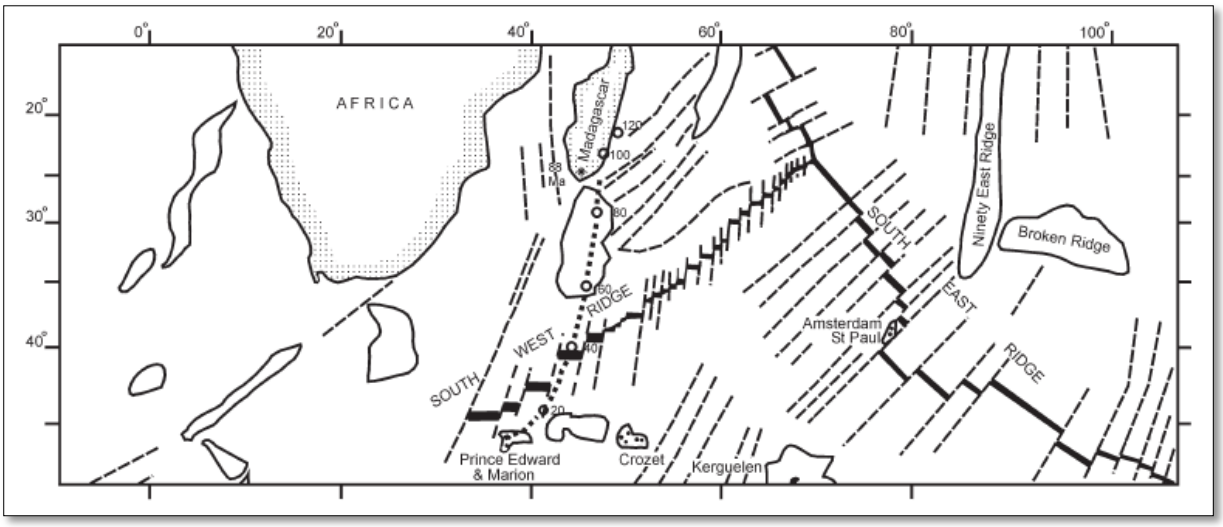

Figure 6.3: A map showing the transform faults radiating from the South West Indian Ridge. Marion Island is positioned southwards along one of the faults. This also shows the hotspot track (the dotted line) which could be responsible for the formation of Marion Island (McDougall *et al.*, 2001).

It only requires a percentile increase in water content of the magma to transition from dry to wet conditions in the mantle. The addition of water to dry systems tends to shift the solidus from higher temperatures to lower temperatures, resulting in an increase in the amount of melt, and also causing significant changes in the order of appearance in crystallising phases (Feig *et al.*, 2006). Hypothetically, water could permeate from a shallow

water reservoir within the crust at depths of up to 15km through fractures which formed as a result of faulting. However, it is highly unrealistic to have so much water propagating such great depths within the mantle. This would only be plausible if the magma chamber was positioned at shallower depths within the Earth's crust. This is also supported by the notion that in order to form a volcanic edifice, magma should be supplied from a crustal magma chamber which is at a shallower depth (Gudmundsson, 2012).

Marion Island has a very distinct tectonic setting. It is seated on top of a transform fault that radiates outwardly from the South West Indian Ocean Ridge (Figure 6.3). Transform fault scarring also occurs in this region extending to great depths within the Earth's mantle. The transform faults are suitable conduits of water into the system at shallow depths within the crust (between 0 and 15km). The water could be sourced from an underground reservoir within the crust or from seawater seeping through the earth's crust in areas where country rock behaves in a brittle manner. This serves as an acceptable conduit for water to enter into the volcanic system and thus triggering a degassing event.

Another important parameter that might need to be taken into consideration is the effect of oxygen fugacity (fO_2). This plays an influential role in the stability of oxide phases, mafic silicates, and minerals depleted in iron. With increasing water content, there is an increase in fO_2, and this in turn has an effect on the stability of minerals. This further suggests that, in the case of Marion Island, the above average water content resulted in the formation of a highly oxidising environment.

CHAPTER 7 – CONCLUSIONS

Several clinopyroxene megacrysts from Pyroxene Hill, which is situated on Marion Island, were studied in order to identify the inclusions present within the samples and to further determine their mineralogical and textural relationships. Their mineralogical and geological constraints in relation to formation mechanisms were also determined and the findings are summarised in this chapter.

Advanced analytical technologies, including microfocus CT, were used to produce 2D and 3D slices of the megacrysts. This assisted in the identification of various inclusions present and in visualising internal structures and textural relationships between the various mineral phases present. Porosity estimations were deliberated using the grey level method and make up roughly 10% of the total volume of the samples. Differences in attenuation coefficients also made it possible to identify various types of inclusions present within the megacrysts. In total, four different mineral phases appeared to have different grey values which range from high (bright white) to low (grey-black). An array of differently shaped olivine crystals were identified within the megacrysts. However, some appeared to have higher grey values than usual. This is attributed to the effect of hematite exsolving along the poor cleavage planes of olivine thus increasing the overall grey values of olivine. Ancillary phases such as Fe-Ti-Al-Cr oxides and sulphides reached the highest grey values. Though these two phases have fairly similar densities which caused them to attenuate in the same manner, their textural properties made it easy to discern between the Fe-oxides, with some occurring as euhedral and fragmented crystals and others forming precipitates within the olivine inclusions. Sulphide blebs are restricted within the walls of clinopyroxene.

Major element data for clinopyroxene strongly suggests that the clinopyroxene is mainly diopsidic with secondary amphibole neck lacing its margins. This phase likely formed by replacement process during cooling of a lava flow. A compilation of clinopyroxenes with a crustal and mantle source were used to delineate the source of these giant megacrysts. Major element data points toward the giant megacrysts having a mid-crustal signature. It forms distinct clusters in regions reflecting a strong crustal signature.

Olivine is derived from shallow mantle depths and affected by dehydrogenation-oxidation process. This process is manifested by the precipitation of hematite along cleavage planes and dislocations of olivine. H was incorporated within the olivine structure thus providing the water needed to precipitate hematite. This process further drives the release of Fe^{3+} from olivine making it more Mg rich. The transfer of olivine to shallower depths, oxidation of Fe^{2+} to Fe^{3+} and long diffusion times led to the precipitation of hematite. Dehydrogenation of olivine has also led to olivine being metamorphosed. Two distinct generations of olivine were identified based upon Ti concentrations of olivine. Early metamorphic olivines are enriched in Ti whilst second generation metamorphic olivine have low Ti concentrations.

Fragmented euhedral crystal of magnetite, chromite, spinel and ilmenite were identified as the Fe-Al-Ti-Cr oxides inclusions in olivine. Their euhedrality and fragmented nature distinguishes them as xenocrystic primary phases which were sourced from the mantle during the early stages of crystallisation. The magnetite and sulphide blebs identified along the olivine-clinopyroxene boundary and in the clinopyroxene megacrysts formed during a cooling of the lava flow.

It can further be concluded that crystal growth is essentially driven by phase disequilibrium in the magmatic system. This prevents the reaction between crystals and magma and thus prohibits the formation of lozenge-shaped clinopyroxene crystals; a common indicator of a crystal quenched by melts during transportation to the earth's surface. Both water and supersaturation of the magmatic system accelerate rapid crystal growth of the Marion Island megacrysts and also restores equilibrium conditions in the system. Though previous authors have described the mantle as being under dry conditions, the exsolutions of hematite and the formation of these giant megacrysts suggest that dehydrogenation-oxidation formation mechanism led to the development of wet conditions in the magmatic system. This water is a crucial phase required in the formation of some of the mineral phases included in the clinopyroxene megacrysts and also making up a considerable fraction of the mantle, furthermore. It is also responsible for triggering the large degassing event required for the rapid growth of the clinopyroxene megacrysts.

CHAPTER 8 – REPERENCES

Anderson, E. M., 1951. *The dynamics of faulting and dyke formation with applications to Britain*. Edinburgh: Oliver and Boyd.

Asimow, P.D. and Langmuir, C.H., 2003. The importance of water to oceanic mantle melting regimes. *Nature*, 421, pp.815-820.

Auzende, A.L., Daniel, I., Reynard, B., Lemaire, C. and Guyot, F., 2004. High-pressure behaviour of serpentine minerals: a Raman spectroscopic study. *Physics and Chemistry of Minerals*, 31(5), pp.269-277.

Battacharya, A., 2012. New model to estimate water in Earth's mantle. *Eos*, 93(32), pp.316.

Bergstrom, D., Hodgson, D.A. and Convey, P., 2006. The physical setting of the Antarctic. In: D.M. Bergstrom, P. Convey and A.H.L. Huiskes,eds. *Trends in Antarctic Terrestrial and Limnetic Ecosystems: Antarctica as a Global Indicator*. Dordrecht: Springer. pp.15-33.

Binns, R.A., Duggan, M.B. and Wilkinson, J.F.G., 1970. High pressure megacrysts in alkaline lavas from northeastern New South Wales. *American Journal of Science*, 269(2), pp.132-168.

Boelhouwers, J.C., Meiklejohn, K.I., Holness, S. and Hedding, D.W., 2008. Geology, geomorphology and climate change. In: S.L. Chown and P.W. Froneman, eds. *The Prince Edward Islands: land-sea interactions in a changing ecosystem.* Stellenbosch: African Sun Media. pp.65-96.

Bogner, A., Jouneau, P.H., Thollet, G., Basset, D., Gauthier, C., 2007. A history of scanning electron microscopy developments: towards ''wet-STEM'' imaging. *Micron;* 38(4), pp.390-401.

Botha, A.E.J., 2013. *Complex zoning in clinopyroxenes from Marion Island.* MSc. University of Pretoria. Available at: <http://repository.up.ac.za/dspace/handle/2263/24752> [Accessed 14 February 2014].

Brugger, C.R. and Hammer, J. E., 2010. Crystallization kinetics in continuous decompression experiments: Implications for interpreting natural magma ascent processes. *Journal of Petrology*, 51(9), pp.1941-1965.

Carter, J.L., 1970. Mineralogy and chemistry of the earth's upper mantle based on the partial fusion-partial crystallization model. *Geological Society of America Bulletin*, 81(7), pp.2021-2032.

Champness, P.E., 1970. Nucleation and growth of iron oxides in olivines, (Mg, Fe) $_2SiO_4$. *Mineralogical Magazine*, 37(291), pp.790-800.

Cooper, J. and Headland, R. K., 1991. A history of South African involvement in Antarctica and at the Prince Edward Islands. *South African Journal of Antarctic Research*, 21, pp.77-91.

Corrigan, G.M., 1982. Supercooling and the crystallization of plagioclase, olivine, and clinopyroxene from basaltic magmas. *Mineralogical Magazine*, 46, pp.31-42.

De Hoog, J.C., Hattori, K. and Jung, H., 2014. Titanium-and water-rich metamorphic olivine in high-pressure serpentinites from the Voltri Massif (Ligurian Alps, Italy): evidence for deep subduction of high-field strength and fluid-mobile elements. *Contributions to Mineralogy and Petrology*, 167(3), pp.1-15.

Deer, W.A., Howie, R.A. and Zussman, J. eds., 1997. *Rock forming minerals: single chain silicates.* 2nd ed. Essex: The Geological Society.

Dyar, M.D., Delaney, J.S., Sutton, S.R. and Schaefer, M.W., 1998. Fe^{3+} distribution in oxidized olivine: A synchrotron micro-XANES study. *American Mineralogist*, 83(12), pp.1361-1365.

Feig, S.T., Koepke, J. and Snow, J.E., 2006. Effect of water on tholeiitic basalt phase equilibria: an experimental study under oxidizing conditions. *Contributions to Mineralogy and Petrology*, 152(5), pp.611-638.

Fipke, C.E., Gurney, J.J., Moore, R.O. and Nassichuk, W.W., 1989. The development of advanced technology to distinguish between diamondiferous and barren diatremes. *Geological Survey of Canada*, 2124, p.559.

Fraser, C.I., Nikula, R., Ruzzante, D.E. and Waters, J. M., 2012. Poleward bound: biological impacts of Southern Hemisphere glaciation. *Trends in Ecology and Evolution*, 27(8), pp.462-471.

Gargiulo, M.F., Bjerg, E.A. and Mogessie, A., 2013. Spinel group minerals in metamorphosed ultramafic rocks from Río de Las Tunas Belt, Central Andes, Argentina. *Geologica Acta*, 11(2), pp.133-148.

Geochemistry of Rocks of the Oceans and Continents (GEOROC), 2016. *Minerals*. [online] Available at: <http://georoc.mpch-mainz.gwdg.de/georoc/> [Accessed 18 August 2016].

Goldstein, J., Newbury, D.E., Echlin, P., Joy, D.C., Romig Jr, A.D., Lyman, C.E., Fiori, C. and Lifshin, E., 2012. *Scanning electron microscopy and X-ray microanalysis: a text for biologists, materials scientists, and geologists*. 2nd ed. New York: Springer Science & Business Media.

Green, D.H. and Ringwood, A.E., 1967. The genesis of basaltic magmas. *Contributions to Mineralogy and Petrology*, 15(2), pp.103-190.

Green, L.G.,1965. *Almost forgotten, never told: A book of the people and places, dramas and adventures along the South African Coast, with a few voyages into deeper waters.* Cape Town: Howard Timmins.

Gudmundsson, A., 2012. Magma chambers: formation, local stresses, excess pressures, and compartments. *Journal of Volcanology and Geothermal Research*, 237-238, pp.19-41.

Hall, K., 1982. Rapid deglaciation as an initiator of volcanic activity: An hypothesis. *Earth Surface Processes and Landforms*, 7(1), pp.45-51.

Hall, K., 2002. Review of present and quaternary periglacial processes and landforms of the maritime and sub-Antarctic region: Periglacial and Permafrost Research in the Southern Hemisphere. *South African Journal of Science*, 98(1-2), pp.71-81.

Hall, K., Meiklejohn, I., and Bumby, A., 2011. Marion Island volcanism and glaciation. Antarctic Science, 23(2), pp.155-163.

Hanesch, M., 2009. Raman spectroscopy of iron oxides and (oxy) hydroxides at low laser power and possible applications in environmental magnetic studies. *Geophysical Journal International*, 177(3), pp.941-948.

Ho, K.S., Chen, J.C., and Juang, W.S., 2000. Geochronology and geochemistry of late Cenozoic basalts from the Leiqiong area, Southern China. *Journal of Asian Earth Sciences*, 18(3), pp.307–324.

Hofmeyr, G.J.G., Bester, M.N. and Jonker, F.C., 1997. Changes in the population sizes and distribution of fur seals at Marion Island. *Polar Biology*, 17(2), pp.150-158.

Huang, X.L., Xu, Y.G, Lo, C.H, Wang, R.C., and Lin, C.Y., 2007. Exsolution lamellae in a clinopyroxene megacryst aggregate from Cenozoic basalt, Leizhou Peninsula, South China: petrography and chemical evolution. *Contributions to Mineralogy and Petrology*, 154(6), pp.691-705.

Hutson T., 2003. Marion and Prince Edward Islands *Ports and Ships*, [online] Available at:<http://ports.co.za/didyouknow/article_2004_04_26_5728.html> [Accessed 26 March 2015].

Hwang, S.L., Yui, T.F., Chu, H.T., Shen, P., Iizuka, Y., Yang, H.Y., Yang, J. and Xu, Z., 2008. Hematite and magnetite precipitates in olivine from the Sulu peridotite: A result of dehydrogenation-oxidation reaction of mantle olivine?. *American Mineralogist*, 93(7), pp.1051-1060.

Ingrin, J. and Skogby, H., 2000. Hydrogen in nominally anhydrous upper-mantle minerals: concentration levels and implications. *European Journal of Mineralogy*, 12(3), pp.543-570.

Irving, A.J., 1974. Megacrysts from the Newer Basalts and other basaltic rocks of Southeastern Australia. *Geological Society of America Bulletin*, 85(10), pp.1503-1514.

Johnson, K., Dick, H.J. and Shimizu, N., 1990. Melting in the oceanic upper mantle: an ion microprobe study of diopsides in abyssal peridotites. *Journal of Geophysical Research: Solid Earth*, 95(B3), pp.2661-2678.

Kaur, H.S., 2006. *Instrumental methods of chemical analysis*. 3rd ed. Meerut: Pragati Prakashan.

Ketcham, R.A. and Carlson., 2001. Acquisition, optimization and interpretation of x-ray computed tomographic imagery: applications to the geosciences. *Computers and Geosciences*, 27(4), pp.381-400.

Khisina, N.R. and Wirth, R., 2002. Hydrous olivine $(Mg_{1-y}\ Fe^{2+}{}_y)_{2-x}\ v_x\ SiO_4H_{2x}$– a new DHMS phase of variable composition observed as nanometer-sized precipitations in mantle olivine. *Physics and Chemistry of Minerals*, 29(2), pp.98-111.

Kimia, B., 2011. *Geometry in CT Reconstruction*.

Kohlstedt, D.L. and Vander Sande, J.B., 1975. An electron microscopy study of naturally occurring oxidation produced precipitates in iron-bearing olivines. *Contributions to Mineralogy and Petrology*, 53(1), pp.13-24.

Krause, S., Bronstert, A. and Zehe, E., 2007. Groundwater–surface water interactions in a North German lowland floodplain–implications for the river discharge dynamics and riparian water balance. *Journal of hydrology*, 347(3), pp.404-417.

le Roex, A. P., Chevallier, L., Verwoed, W.J. and Barends, R., 2012. Petrology and geochemistry of Marion and Prince Edward Islands, Southern Ocean: Magma chamber processes and source region characteristics. *Journal of Volcanology and Geothermal Research*, 223, pp.11-28.

le Roex, P.C. and McGeoch, M. A., 2008. Changes in climate extremes, variability and signature on sub-Antarctic Marion Island. *Climatic Change*, 86(3), pp.309-329.

Leake, B.E., Woolley, A.R., Arps, C.E., Birch, W.D., Gilbert, M.C., Grice, J.D., Hawthorne, F.C., Kato, A., Kisch, H.J., Krivovichev, V.G. and Linthout, K., 1997. Nomenclature of Amphiboles: report of the subcommittee on amphiboles of the international mineralogical association commission on new minerals and mineral names. *Mineralogical Magazine*, 61(2), pp.295-321.

Lorand, J.P., Alard, O., Luguet, A. and Keays, R.R., 2003. Sulfur and selenium systematics of the subcontinental lithospheric mantle: inferences from the Massif Central xenolith suite (France). *Geochimica et Cosmochimica Acta*, 67(21), pp.4135–4151.

Mahoney, J., le Roex, A.P., Peng, Z., Fisher, R.L. and Natland, J. H., 1992. Southwestern limits of Indian Ocean ridge mantle and the origin of low $^{206}Pb/^{204}Pb$ mid-ocean ridge basalt: Isotope systematics of the central Southwest Indian Ridge (17°–50°E). *Journal of Geophysical Research*, 97(B13), pp.19771-19790.

Markowicz, A.A., 1993. X-ray physics. In. R.E. Van Grieken, A.A. Markowicz, eds.2001. *Handbook of X-ray Spectrometry*. New York: Marcel Dekker. pp.1-99.

Marsh, J.H., 1948. *No Pathway Here*. Cape Town: Howard Timmins.

McDougall, I., Verwoerd, W. and Chevallier, L., 2001. K-Ar geochronology of Marion Island, Southern Ocean. *Geological Magazine*, 138(1), pp.1-17.

Mees, F., Swennen, R., Van Geet, M. and Jacobs, P., 2003. Applications of X-ray computed tomography in the geosciences. *The Geological Society of London, Special Publications*, 215(1), pp.1-6.

Morimoto, N., 1988. Nomenclature of pyroxenes. *Mineralogy and Petrology*, 39(1), pp.55-76.

Müssig J. ed., 2010. *Industrial Applications of natural fibres: structure, properties and technical applications*. Chichester: John Wiley & Sons.

Nesse,W.D., 2000. *Introduction to Mineralogy*. New York: Oxford University Press.

Nimis, P. and Taylor, W.R., 2000. Single clinopyroxene thermobarometry for garnet peridotites. Part I. Calibration and testing of a Cr-in-Cpx barometer and an enstatite-in-Cpx thermometer. *Contributions to Mineralogy and Petrology*,139(5), pp.541-554.

Pasteris, J.D., Freeman, J.J., Goffredi, S.K. and Buck, K.R., 2001. Raman spectroscopic and laser scanning confocal microscopic analysis of sulfur in living sulfur-precipitating marine bacteria. *Chemical Geology*, 180(1), pp.3-18.

Peterson, R., and Francis, D., 1977. The origin of sulfide inclusions in pyroxene megacrysts. *American Mineralogist*, 62(9-10), pp.1049-1051.

Potgieter, D.J. and DuPlessis, P.C. eds., 1970. *Standard Encyclopaedia of Southern Africa, Volume1*. Cape Town: NASOU.

Prinsloo, L.C., Colomban, P., Brink, J.D. and Meiklejohn, I., 2010. A Raman spectroscopic study of the igneous rocks on Marion Island: a possible terrestrial analogue for the geology on Mars. *Journal of Raman Spectroscopy*, 42(4), pp.626-632.

Prokop, J., Švéda, L., Jančárek, A. and Pína, L., 2009. Porosity measurement method by X-ray computed tomography. *Key Engineering Materials*, 409, pp.402-405.

Putnis, A., 1992. *An introduction to mineral sciences*. Cambridge: Cambridge University Press.

Quirt, D.H., 2004. Cr-diopside (clinopyroxene) as a kimberlite indicator mineral for diamond exploration in glaciated terrains; in Summary of Investigations 2004. *Saskatchewan Geological Survey*, 2, pp.1-14.

Raman, C.V. and Krishnan, K.S., 1928. A new type of secondary radiation. *Nature*, 121(3048), pp.501-502.

Schulze, D.J. (1987). Megacrysts from alkalic volcanic rocks. In P.H. Nixon, ed. 1987. *Mantle xenoliths*. New York: John Wiley. pp.433-451.

Selyatitskii, A.Y. and Reverdatto, V.V., 2011. Comparison of the compositions of olivines and clinopyroxenes from mantle and "crustal" peridotites of collisional high-pressure/ultrahigh-pressure zones. *Doklady Earth Sciences*, 438(1), pp.705-710.

South African National Antarctic Programme (SANAP), 2015a. *Marion Island: Overview*. [online] Available at: <http://www.sanap.ac.za/sanap_marion/sanap_marion.html> [Accessed 12 March 2015].

South African National Antarctic Programme (SANAP), 2015b. *Marion Island: History*. [online] Available at: <http://marion.sanap.org.za/history.html> [Accessed 12 March 2015].

South African National Antarctic Programme (SANAP), 2015c. *Marion Island: Life at the base*. [online] Available at: <http://www.sanap.ac.za/sanap_marion/marion_life_at_the_base.html> [Accessed 12 March 2015].

Stearns, H.T. and Macdonald, G.A., 1942. *General geology and ground-water resources of the island of Maui, Hawaii, Bulletin 7*.[pdf] Honolulu: Advertiser Publishing Co. Available at: <https://pubs.usgs.gov/misc/stearns/Maui.pdf> [Accessed: 5 May 2016].

Storey, M., Mahoney, J.J., Saunders, A.D., Duncan, R.A., Kelley, S.P. and Coffin, M.F., 1995. Timing of hot spot-related volcanism and the breakup of Madagascar and India. *Science*. 267(5199), pp.825-855.

Streck, M.J., 2008. Mineral textures and zoning as evidence for open system processes. *Reviews in Mineralogy and Geochemistry*, 69(1), pp.595-622.

Suppe, J., 1985. *Principles of Structural Geology*. New Jersey: Prentice-Hall.

Swapp, S., 2012. Scanning electron microscopy (SEM).*Geochemical Instrumentation and Analysis*. [online] Available at: <http://serc.carleton.edu/research_education/geochemsheets/techniques/SEM.html > [Accessed 15 May 2016].

Taud, H., Martinez-Angeles, R., Parrot, J.F. and Hernandez-Escobedo, L., 2005. Porosity estimation method by X-ray computed tomography. *Journal of Petroleum Science and Engineering*, 47(3), pp.209-217.

Van Geet, M., Swennen, R. and Wevers, M., 2000. Quantitative analysis of reservoir rocks by microfocus x-ray computerised tomography. *Sedimentary Geology*, 132(1), pp.25-36.

Verwoerd, W.J., 1971. Geology. In: E.M. Van Zinderen Bakker, J.M. Sr, Winterbotton, and R.A Dyer, eds. 1971. *Marion and Prince Edward Islands. Report on the South African Biological & Geological Expedition / 1965-1966*. Cape Town: A.A Balkema. pp.40-62.

Verwoerd, W.J., Russell, S. and Berruti, A., 1981. 1980 Volcanic eruption reported on Marion Island. *Earth and Planetary Science Letters*. 54(1), pp.153-156.

Welsch, B., Hammer, J., Baronnet, A., Jacob, S., Hellebrand, E. and Sinton, J., 2016. Clinopyroxene in postshield Haleakala ankaramite: 2. Texture, compositional zoning and supersaturation in the magma. *Contributions to Mineralogy and Petrology*, 171(1), pp.1-19.

White, R.W., 1966. Ultramafic inclusions in basaltic rocks from Hawaii. Contributions to Mineralogy and Petrology, 12(3), pp.245-314.

Willard, H.H., Merritt, L.L. Jr., Dean, J.A. and Settle, F.A., 1988. *Instrumental Methods of Analysis*. 7th ed. Florence: Wadsworth Publishing Company.

Woodland, A.B., and Jugo, P.J., 2007. A complex magmatic system beneath the Deves volcanic field, Massif Central, France: evidence from clinopyroxene megacrysts. *Contributions to Mineralogy and Petrology*, 153(6), pp.719-731.

Yu, J.H., O'Reilly, S.Y., Griffin, W.L., Xu, X., Zhang, M. and Zhou. X., 2003.The thermal state and composition of the lithospheric mantle beneath the Leizhou Penisula, South China. *Journal of Volcanology and Geothermal Research*, 122(3), pp.165–189.